PHYSICAL REVIEW B **108**, 094303 (2023)

Scattering quantum walk framework for two-dimensional materials: The case of honeycomb lattice structures

B. F. Venancio,[1,*,†] H. S. Ghizoni,[2,*,‡] and M. G. E. da Luz[2,§]
[1]*Instituto Federal do Paraná, 80230-150 Curitiba-PR, Brazil,*
[2]*Departamento de Física, Universidade Federal do Paraná, 81531-980 Curitiba-PR, Brazil*

(Received 10 June 2023; accepted 6 September 2023; published 13 September 2023)

Bidimensional crystals display unique properties of both fundamental and applied interest, with a good part of these properties being related to the topological aspects of 2D materials. Discrete quantum walks models, commonly used in the area of quantum information, are mathematical constructions in which the underlying network topology plays a fundamental role in determining the systems behavior. Here we present a complete scattering quantum walks approach to study 2D honeycomb lattice problems, the structure of paradigmatic 2D Dirac materials like graphene, germanene and silicene. The framework great flexibility relies on considering two arbitrary 3×3 unitary scattering matrices $\hat{\Gamma}^{(\pm)}$ to describe the local dynamics in the lattice fundamental cell. From a simple analytic choice for $\hat{\Gamma}^{(\pm)}$, we address important aspects of 2D materials like transport characteristics. We also readily obtain analytic formulas for quantities which are commonly derived from a tight-binding approximation. Most importantly, we derive a rather general equation for the system energy bands based on the determinant of products of $\hat{\Gamma}^{(\pm)}$. We show that by properly setting these matrices (numerically), we get good agreements between our calculations for the π and π^* energy bands of the graphene, germanene and siliciene with accurate *ab initio* methods in the literature. We finally briefly discuss how the $\hat{\Gamma}^{(\pm)}$ could be computed from first principles, making the present an useful protocol to investigate 2D materials.

DOI: 10.1103/PhysRevB.108.094303

I. INTRODUCTION

More prominently since the 1980s [1–4], the realization that topological factors can deeply determine key traits in condensed matter physics has considerably enlarged our understanding of matter aggregation and organization [5–8]. Indeed, topology-induced properties and/or processes are able to explain, e.g., phase transitions without symmetry breaking [9,10], band gaps remaining finite along adiabatic paths in parameter space [11], transport coefficients dependent on topological invariants [12], and fractional charges [11], to cite just few examples. All these features have motivated the search for different materials with various fundamental and applied purposes [7,9,10,13,14].

In particular, 2D materials are systems for which topology is especially significant in determining some of their fundamental characteristics [9,12,15,16]. It is also representative that certain topological states in 3D solids have as origin-embedded 2D layered motifs [17,18]. There are different reasons for the relevance of topological effects in 2D structures (a good summary is given in Ref. [19]). We mention, e.g., the great interplay between symmetry and topology in planar materials [19,20].

Graphene, one of the best known and studied two-dimensional stable crystals [21–32], is not an exception to the aforementioned scenario [33]. It consists of a monolayer of sp^2 hybridized carbon atoms arranged in a regular hexagonal (honeycomb) infinite lattice. Graphene displays remarkable electronic features. It is a semimetal allowing ballisticlike spreading of electrons [21,22]. Further, the graphene valence and conductance bands touch at Dirac (or Brillouin zone K) points, resembling massless fermions with a dispersion relation linear around K. More broadly, it belongs to the important class of 2D Dirac materials [34], part of them also presenting a hexagonal structure as germanene and silicene [35–38]. In fact, graphene, germanene and silicene are akin in other aspects. For instance, when "cut" in finite sheets (nanoribbons), all them behave either as conductors or semiconductors, depending on the geometry specific boundary conditions, respectively, zigzag or armchair.

As expected, distinct methods (some computationally expensive) have been proposed, including *ab initio* and semiempirical approaches, to calculate several properties of Dirac materials (for general discussions see, e.g., Refs. [39,40]). Nonetheless, it has been argued [33,41,42] that important aspects of these systems might be inferred from their pure geometric and topological structures. Of course, the actual chemical species and chemical bond specificities are fundamental [43]. But, eventually, they could be treated effectively, as a parametric dynamical factor incorporated into the model description. Hence, one could consider topologically oriented theoretical schemes to address characteristics like transport and energy bands of Dirac systems, notably in honeycomb lattices [44–47].

Quantum walks (QWs) constitute a simple and versatile mathematical framework along the above lines. Indeed, it is

---

[*] These authors contributed equally to this paper.

[†] bruno.venancio@ifpr.edu.br

[‡] henrique_ghizoni@hotmail.com

[§] Corresponding author: luz@fisica.ufpr.br based on network (and thus topological) concepts and constructed using minimal rules of quantum mechanics [48–51]. Although finding distinct applications, like in cold atoms trapping [52], molecular physics [53–55], and quantum optics [56–58], by far the most common usage of QWs (in its so-called coin formulation) is in quantum information and computation [59–62]. Distinct works have also employed QWs to analyze 2D materials, nevertheless usually focusing just in specific aspects of the problem. For a glimpse see, e.g., the Refs. [44,45,47,63,64].

Considering the somehow more physically intuitive scattering formulation for quantum walks (SQWs) [65–67]—actually, it has been proven that coin and scattering QWs are always unitarily equivalent [68], although the mapping may be involved—recently, all the possible discrete time SQW models in a plain (identical vertices) hexagonal lattice have been classified [46]. In the present contribution, we show that one of these SQW versions is particularly suitable to describe 2D Dirac materials in a honeycomb lattice.

We first review the basic formalism in the configuration space of a proper SQW on a honeycomb (infinite) lattice, also addressing its general properties, Secs. II and III. Then we turn to the momentum space, deriving a general equation which yields the problem energy-band structures. Such expression is based on two arbitrary U(3) scattering matrices, $\hat{\Gamma}^{(+)}$ and $\hat{\Gamma}^{(-)}$, whose particular parameter values should be defined depending on each specific 2D system, Sec. IV. By a simple choice for these matrices, we can obtain in a rather straightforward way known analytic results as the tight-binding approximation (in fact, going beyond it) and a formula for the Fermi velocity, Sec. V. Different analysis for actual materials—more extensively for graphene, but also for germanene and silicene—are performed. Especially, we illustrate that from appropriate $\hat{\Gamma}^{(+)}$ and $\hat{\Gamma}^{(-)}$, we get the π and π^* energy bands displaying very good agreement with accurate *ab initio* computations in the literature, Sec. VI. Final remarks, including a brief discussion of how the scattering matrices might be inferred from first-principles calculations, are given in Sec. VII. Certain derivations and protocols are left to Appendices A–C.

II. THE SQW IN A HONEYCOMB LATTICE

A thorough description of how to formulate distinct SQW models in a honeycomb lattice has been presented in Ref. [46]. In the following, we summarize only the essential ingredients necessary for our goals in this contribution.

The honeycomb topological structure is depicted in Fig. 1(a), where each pair (j, k) of integers represents a site (vertex). The corresponding Cartesian coordinates are [with a the bond (edge) length]

$$x_j = \frac{\sqrt{3}\, j}{2} a, \quad y_k = \left(\frac{3k}{4} + \frac{9 - (-1)^k}{8}\right) a. \tag{1}$$

The basic structure used to define local scattering processes as well as the σ labeling convention for its bonds (or links)—along which we assume two propagation directions—are shown in Fig. 1(b).

The problem Hilbert space is spanned by the orthonormal basis $\{|\sigma, j, k\rangle\}$, representing a propagation toward the site (j, k) along the bond $\sigma = 1, 2, 3$, so

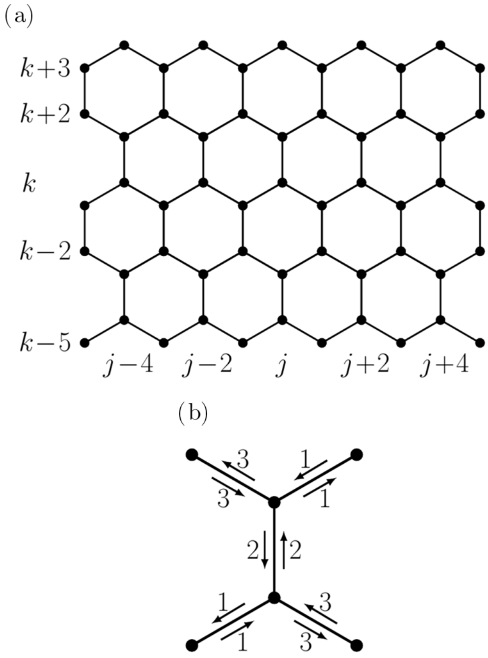

FIG. 1. (a) The honeycomb lattice. Without loss of generality, the k's indicating the sites with one up and two down bonds are assumed even numbers. (b) The reference structure used to label (as indicated) the propagation direction quantum number $\sigma = 1, 2, 3$. Along each bond, two directions are possible.

$$\langle\sigma', j', k'|\sigma, j, k\rangle = \delta_{\sigma'\sigma}\delta_{j'j}\delta_{k'k},$$
$$\hat{\mathbf{1}} = \sum_{\sigma=1}^{3}\sum_{j,k} |\sigma, j, k\rangle\langle\sigma, j, k|. \tag{2}$$

At discrete steps n (e.g., for the instant t_n, we can assume $t_n = n\,\tau$ for $n \in \mathbb{N}$ and τ a typical time interval) we have that

$$|\psi_n\rangle = \hat{U}^n|\psi_0\rangle \tag{3}$$

for $|\psi_0\rangle$ the system initial state. The action of $\hat{U}$ on $|\sigma, j, k\rangle$ yields

$$\hat{U}|\sigma, j, k\rangle = \sum_{\sigma'=1}^{3} \Gamma_{\sigma'\sigma}^{(j,k)}\, |\sigma', \mathcal{J}(\sigma', j, k), \mathcal{K}(\sigma', j, k)\rangle, \tag{4}$$

where $\mathcal{J}(\sigma', j, k)$ and $\mathcal{K}(\sigma', j, k)$ indicate the adjacent sites to (j, k) through the direction σ', or

$$\mathcal{J}(\sigma, j, k) = j + (\sigma - 2)(-1)^k,$$
$$\mathcal{K}(\sigma, j, k) = k + (-1)^{k+\sigma}. \tag{5}$$

Above, the $\Gamma_{\sigma'\sigma}^{(j,k)}$'s are matrix elements (of $\hat{\Gamma}^{(j,k)}$), describing all the scattering processes that the particle can suffer: $\Gamma_{\sigma'\sigma}^{(j,k)}$ is the scattering amplitude from the bond σ to the bond σ' through the site (j, k). Moreover, from the unitarity of $\hat{U}$,

$$\sum_{\sigma=1}^{3} \Gamma_{\sigma\sigma'}^{(j,k)}\, \Gamma_{\sigma\sigma''}^{(j,k)*} = \sum_{\sigma=1}^{3} \Gamma_{\sigma'\sigma}^{(j,k)*}\, \Gamma_{\sigma''\sigma}^{(j,k)} = \delta_{\sigma'\sigma''}, \tag{6}$$

so for any (j,k),

$$\hat{\Gamma}^{(j,k)} = \begin{pmatrix} \Gamma_{11}^{(j,k)} & \Gamma_{12}^{(j,k)} & \Gamma_{13}^{(j,k)} \\ \Gamma_{21}^{(j,k)} & \Gamma_{22}^{(j,k)} & \Gamma_{23}^{(j,k)} \\ \Gamma_{31}^{(j,k)} & \Gamma_{32}^{(j,k)} & \Gamma_{33}^{(j,k)} \end{pmatrix} = \begin{pmatrix} r_{11}^{(j,k)} & t_{12}^{(j,k)} & t_{13}^{(j,k)} \\ t_{21}^{(j,k)} & r_{22}^{(j,k)} & t_{23}^{(j,k)} \\ t_{31}^{(j,k)} & t_{32}^{(j,k)} & r_{33}^{(j,k)} \end{pmatrix}, \quad (7)$$

is a U(3) unitary matrix, whose main diagonal elements are associated to reflection and all the others to transmission coefficients.

For the system state at the n time step being $|\psi_n\rangle$, the probability to find the particle in the site (j,k) simply reads

$$p(j,k,n) = \sum_{\sigma=1}^{3} |\langle\sigma, j, k|\psi_n\rangle|^2 = \sum_{\sigma=1}^{3} |\psi_\sigma(j,k;n)|^2, \quad (8)$$

where $|\psi_n\rangle = \sum_{\sigma,j,k} \psi_\sigma(j,k;n)\,|\sigma, j, k\rangle$. Thus, we define the probability distributions of the j and k coordinates at n, $p_x(j,n)$ and $p_y(k,n)$, as

$$p_x(j,n) = \sum_k p(j,k,n), \qquad p_y(k,n) = \sum_j p(j,k,n). \quad (9)$$

Further, we can determinate the QW mean squared displacement (MSD) as $(r_{(j,k)} = \sqrt{x_j^2 + y_k^2})$,

$$D_x = \sum_j p_x(j,n)\,x_j^2 - \left(\sum_j p_x(j,n)\,x_j\right)^2, \quad (10)$$

$$D_y = \sum_k p_y(k,n)\,y_k^2 - \left(\sum_k p_y(k,n)\,y_k\right)^2, \quad (11)$$

$$D_r = \sum_{j,k} p(j,k,n)\,r_{(j,k)}^2 - \left(\sum_{j,k} p(j,k,n)\,r_{(j,k)}\right)^2. \quad (12)$$

Since QWs generally display superdiffusion, in fact, ballistic behavior, one may expect the following scaling for D_r (see, e.g., Refs. [51,69,70]):

$$D_r = K\,t_n^2 = K\,\tau^2\,n^2, \quad (13)$$

where K should depend only on the matrices' $\hat{\Gamma}$'s parameters. The correctness of the above ansatz will be tested for an explicit example in the next section.

III. A SYMMETRIC EXAMPLE OF $\hat{\Gamma}^{(j,k)}$ AND THE RESULTING DYNAMICS

There is a great freedom in choosing $\hat{\Gamma}^{(j,k)}$. The most general case in which all the reflection coefficients are equal, likewise for all the transmissions, is described by the following two-parameter unitary matrix:

$$\hat{\Gamma}_{AB}(\theta,\gamma) = \exp[i\,\gamma] \begin{pmatrix} r_A(\theta) & t_B(\theta) & t_B(\theta) \\ t_B(\theta) & r_A(\theta) & t_B(\theta) \\ t_B(\theta) & t_B(\theta) & r_A(\theta) \end{pmatrix}, \quad (14)$$

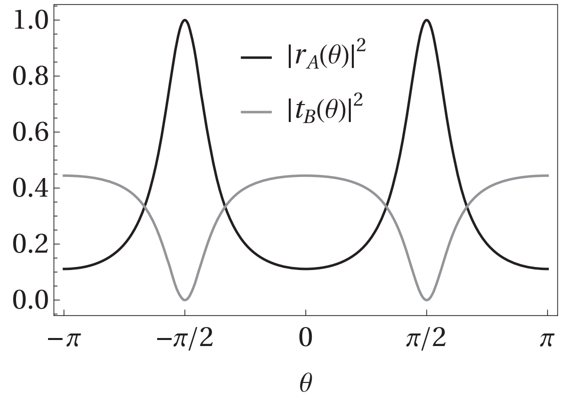

FIG. 2. The modulus square of the reflection and transmission coefficients of $\hat{\Gamma}_{AB}(\theta,\gamma)$ in Eq. (14) as function of θ.

with $(-\pi \leqslant \theta \leqslant \pi)$:

$$r_A(\theta) = -\frac{\exp[i\,\theta]}{\sqrt{5 + 4\cos[2\theta]}}, \quad t_B(\theta) = \frac{2\cos[\theta]}{\sqrt{5 + 4\cos[2\theta]}}. \quad (15)$$

The plots of $|r_A|^2$ and $|t_B|^2$ as function of θ are shown in Fig. 2. Note that $|r_A|^2 = 1$ for $\theta = \pm\pi/2$, with a minimum reflection at $\theta = 0, \pm\pi$ when $|r_A(\theta)|^2 = 1/9$ and $|t_B(\theta)|^2 = 4/9$. For $\theta = \gamma = 0$, the above $\hat{\Gamma}$ is the so-called Grover matrix, widely implemented in quantum search algorithms and in some models of QW [71–74].

For the following examples, in our expression for $\hat{U}$ in Eq. (4), we assume that for any (j,k) we have $\hat{\Gamma}^{(j,k)} = \hat{\Gamma}_{AB}$. We also set

$$|\psi_0\rangle = \frac{1}{\sqrt{3}} \sum_{\sigma=1}^{3} |\sigma, 0, 0\rangle. \quad (16)$$

The resulting evolution at $n = 200$ is shown in Fig. 3 for distinct values of the parameter θ. The plots display the normalized probabilities to be in each site (j,k). Notice that the rotation and inversion point symmetries of the observed patterns are a natural consequence of the system underlying triangular Bravais lattice structures (for details, see Sec. IV). However, this becomes explicit in the present case only due to the specific symmetry of the scattering matrix $\hat{\Gamma}_{AB}$ and the particular initial state chosen, Eq. (16). For a comprehensive discussion about morphologies of general $|\psi_n\rangle$'s, see Ref. [46]. Further, for θ approaching $\pi/2$, the probability distribution tends to be more and more concentrated around the originally populated ring [represented by Eq. (16)]. In fact, for $\theta \to \pm\pi/2$ we have $|r_A(\theta)|^2 \to 1$ (and $|t_B(\theta)|^2 \to 0$), leading to a full localization for the evolved quantum state.

We also investigate the radial MSD, Eq. (12). Figure 4(a) [Fig. 4(b)] displays D_r versus n (D_r versus θ) for different values of the parameter θ (time step n). In Fig. 4(a), we observe the expected ballistic behavior of QW's, i.e., $D_r \propto n^2$ for long n's [62]. The general trend of D_r versus θ in Fig. 4(b) resembles that of the transmission probability $|t_B(\theta)|^2$ seen in Fig. 2. In Fig. 5, we depict $D_r/(a\,n)^2$ as a function of θ for different values of the time step n. Note that even for short n's, such a quantity is fairly independent on time as predicted

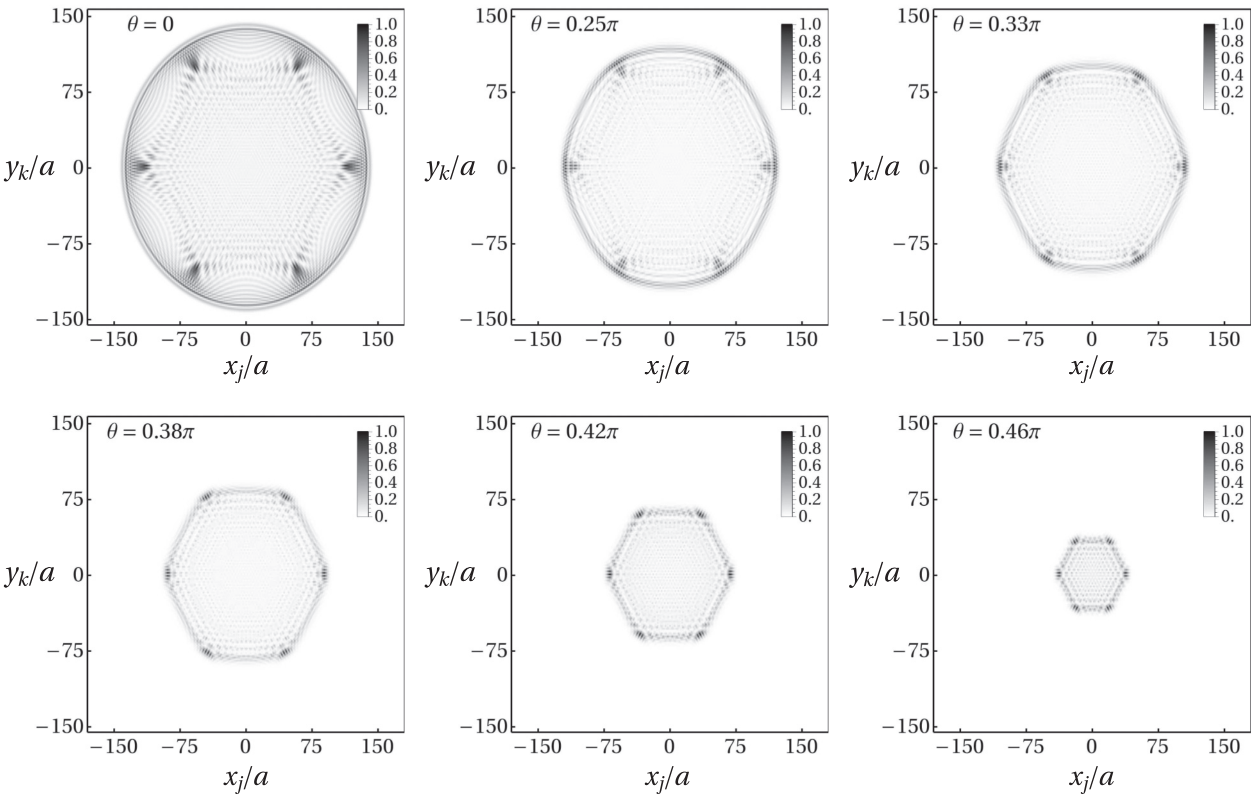

FIG. 3. For all $\hat{\Gamma}^{(j,k)} = \hat{\Gamma}_{AB}$, the normalized probabilities to be at the sites (j, k) obtained from $|\psi_{200}\rangle$ [with $|\psi_0\rangle$ in Eq. (16)] for different θ values.

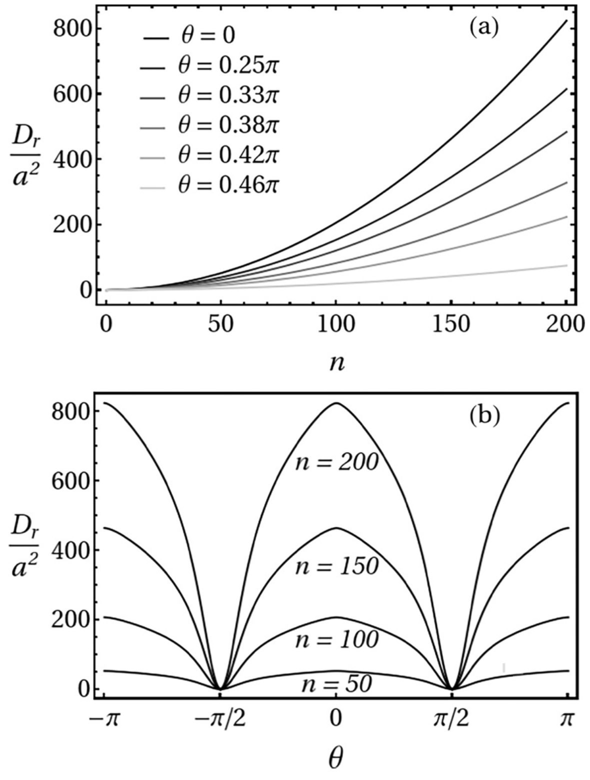

FIG. 4. For the conditions in Fig. 3, the radial D_r, Eq. (12), as function of (a) n for distinct θ and (b) θ for distinct n.

by Eq. (13). So, we propose the following general fitting for $K(\theta)$ [cf. Eq. (13)]:

$$K(\theta) = \frac{a^2}{\tau^2}\,|t_B(\theta)|^2 \sum_{m=0}^{\infty} b_{2m}\,\cos^{2m}[\theta], \tag{17}$$

where the b_{2m}'s are parameters to be adjusted. By truncating Eq. (17) up to $m = 2$, one finds $b_0 = 3.42 \times 10^{-2}$, $b_2 = 4.95 \times 10^{-3}$, and $b_4 = 6.78 \times 10^{-3}$. In Figs. 6 and 7, we show the difference between the numerically calculated $K(\theta)$ and Eq. (17) with such $m = 2$ truncation. Overall, one finds reasonably good agreement between the actual MSD D_r and the present fitting approximation.

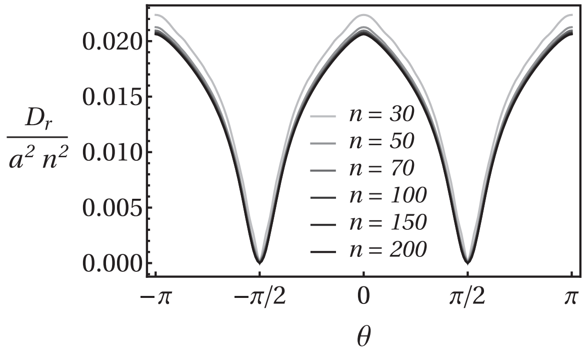

FIG. 5. For the conditions in Fig. 3, plots of $D_r/(a^2n^2)$ versus θ for distinct n (recall that $t_n = n\,\tau$).

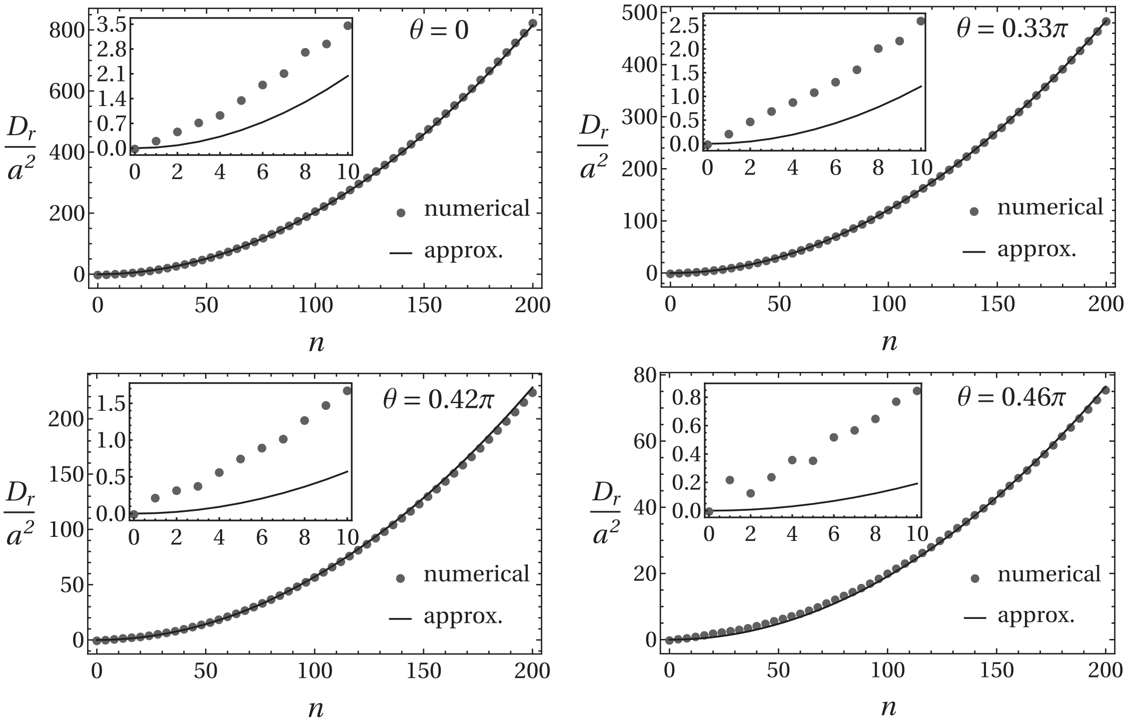

FIG. 6. For the conditions in Fig. 3, plots of D_r/a^2 versus n for different θ's, either from the actual time evolution (numerical) or from $D_r = K^2 t_n^2$ for $K(\theta)$ given in the fitting Eq. (17), truncated up to $m = 2$ (approx.). Some discrepancy appears when $\theta \to \pi/2$. The insets highlight the behavior of D_r/a^2 in the first time steps.

IV. SQW IN THE MOMENTUM SPACE: ENERGY BANDS

As is well-known [75], the honeycomb can be mapped into a triangular Bravais lattice, but with two nonequivalent sites in its fundamental cell, Fig. 8. In this way, the sites (j, k) corresponding to the associated two infinite sublattices (named even and odd) are those having even and odd values

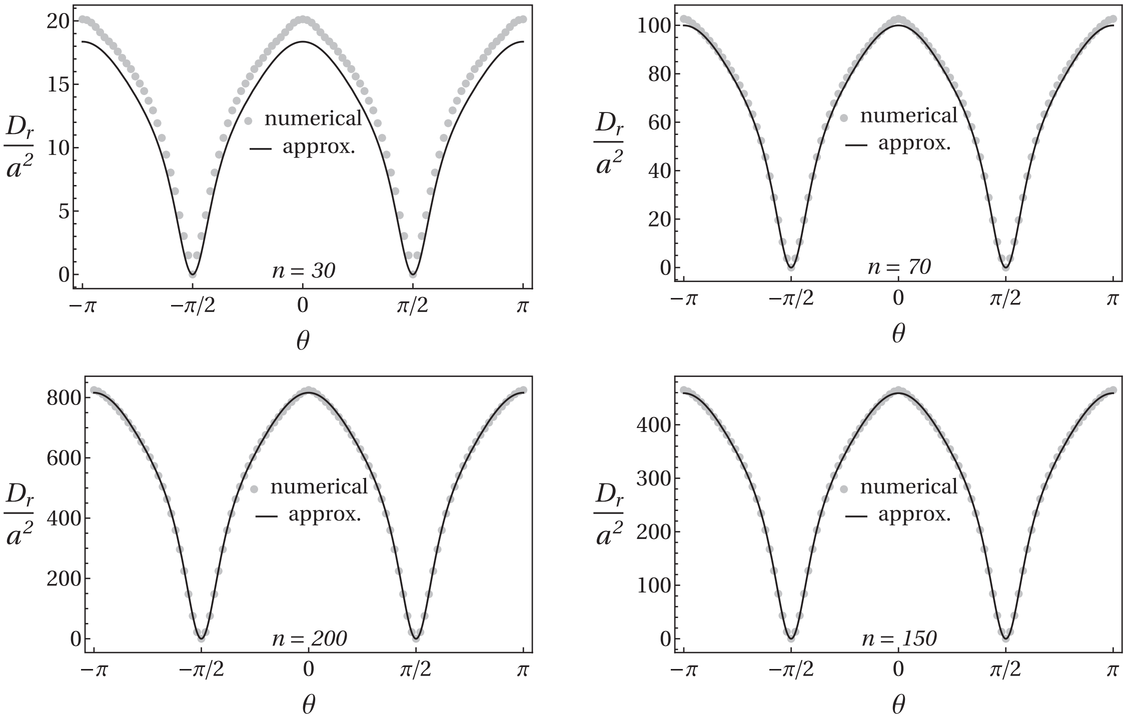

FIG. 7. Similar to Fig. 6, but for D_r/a^2 versus θ for different n's. The curves display discrepancies only for small n's (see also the insets in Fig. 6).

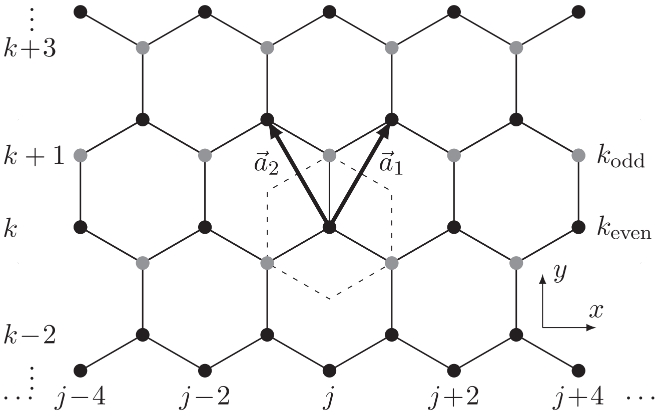

FIG. 8. The mapping of hexagonal lattice sites (black points) onto a triangular Bravais lattice (gray points). The area enclosed by the dashed line represents the Wigner-Seitz cell (WSc), whose translations by vectors $\vec{R}_{(m_1,m_2)}$—perpendicular to the WSc sides—cover the whole plane. The WSc contains two sites, both having the same j coordinate. However, one of even and the other of odd k coordinates.

for k. By setting the basic vectors as

$$\vec{a}_1 = \frac{a}{2}(\sqrt{3}\hat{e}_x + 3\hat{e}_y), \quad \vec{a}_2 = \frac{a}{2}(-\sqrt{3}\hat{e}_x + 3\hat{e}_y), \tag{18}$$

the Bravais lattice is generated by $\vec{R}_{(m_1,m_2)} = m_1\,\vec{a}_1 + m_2\,\vec{a}_2$, with (m_1, m_2) integers. Furthermore, for

$$\vec{b}_1 = \frac{2\pi}{a}\left(\frac{1}{\sqrt{3}}\hat{e}_x + \frac{1}{3}\hat{e}_y\right), \quad \vec{b}_2 = \frac{2\pi}{a}\left(-\frac{1}{\sqrt{3}}\hat{e}_x + \frac{1}{3}\hat{e}_y\right), \tag{19}$$

the reciprocal lattice is generated by $\vec{G}_{(m_1,m_2)} = m_1\vec{b}_1 + m_2\vec{b}_2$. In Fig. 9, we illustrate a small region of the (infinite) reciprocal lattice, indicating the basic directions κ_x and κ_y.

To comply with the system's perfect crystal symmetry, we assume the SQW to be invariant under translations by the vector $\vec{R}_{(m_1,m_2)}$. This implies that

$$\Gamma^{(j,k)}_{\sigma'\sigma} = \Gamma^{(j+m_1-m_2,k+2\,(m_1+m_2))}_{\sigma'\sigma}. \tag{20}$$

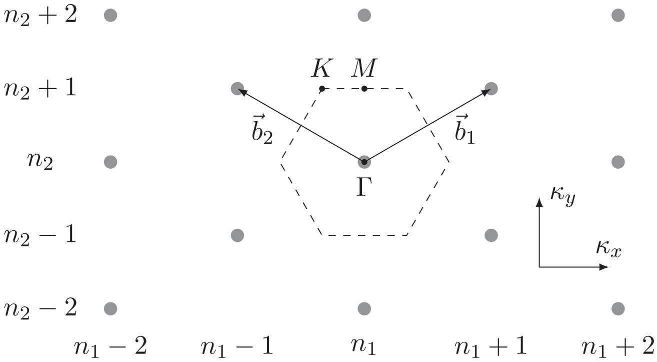

FIG. 9. The reciprocal associated with the Bravais lattice of Fig 8. Akin to the direct lattice, it is also triangular. The area enclosed by the dashed hexagon delimits the first Brillouin zone. The points of high symmetry, Γ, K, and M, have, respectively, the coordinates, (0,0), $(-\frac{2\pi}{3\sqrt{3}a}, \frac{2\pi}{3a})$ and $(0, \frac{2\pi}{3a})$.

Therefore, from Eq. (20) we find that the problem admits just two possible distinct matrices, one for the sites with even k's, $\Gamma^{(j,k_{\text{even}})}_{\sigma'\sigma} = \Gamma^{(+)}_{\sigma'\sigma}$, and the other for the sites with odd k's, $\Gamma^{(j,k_{\text{odd}})}_{\sigma'\sigma} = \Gamma^{(-)}_{\sigma'\sigma}$, or

$$\hat{\Gamma}^{(j,k)} = \hat{\Gamma}^{((-1)^k)}. \tag{21}$$

We now introduce the translation operator, whose action on a position state is

$$\hat{T}_{\vec{R}_{(m_1,m_2)}}\,|\vec{r}\rangle = |\vec{r} + \vec{R}_{(m_1,m_2)}\rangle. \tag{22}$$

Then

$$\begin{aligned}\hat{T}_{\vec{R}_{(m_1,m_2)}} &= \exp[i\,\hat{\vec{K}} \cdot \vec{R}_{(m_1,m_2)}]\\ &= \exp\left[i\,\frac{3}{2}\,a\left(\frac{(m_1-m_2)}{\sqrt{3}}\,\hat{K}_x + (m_1+m_2)\,\hat{K}_y\right)\right],\end{aligned} \tag{23}$$

where $\hat{K}_w = \hat{P}_w/\hbar$, for $\hat{P}_w$ the momentum operator in the $w = x, y$ direction. By defining (with $\mathcal{N}$ a normalization constant)

$$\begin{aligned}|\sigma, \kappa_x, \kappa_y\rangle &= \frac{1}{\mathcal{N}}\sum_j\sum_k \exp[i\,(\kappa_x\,x_j + \kappa_y\,y_k)]\,|\sigma, j, k\rangle\\ &= \frac{1}{\mathcal{N}}\sum_j\sum_{k_{\text{even}}} \exp[i\,(\kappa_x\,x_j + \kappa_y\,y_k)]\,|\sigma, j, k\rangle\\ &\quad + \frac{1}{\mathcal{N}}\sum_j\sum_{k_{\text{odd}}} \exp[i\,(\kappa_x\,x_j + \kappa_y\,y_k)]\,|\sigma, j, k\rangle,\\ &= |\sigma, \kappa_x, \kappa_y\rangle_{\text{even}} + |\sigma, \kappa_x, \kappa_y\rangle_{\text{odd}},\end{aligned} \tag{24}$$

we have that

$$\hat{K}_w\,|\sigma, \kappa_x, \kappa_y\rangle = \kappa_w\,|\sigma, \kappa_x, \kappa_y\rangle. \tag{25}$$

The operator $\hat{T}_{\vec{R}_{(m_1,m_2)}}$ takes sites in the even (odd) sublattice to sites in the even (odd) sublattice. Then, $|\sigma, \kappa_x, \kappa_y\rangle_{\text{even}}$ and $|\sigma, \kappa_x, \kappa_y\rangle_{\text{odd}}$ are degenerate eigenstates of $\hat{K}_w$.

To derive the 2D lattice system energy bands, as usual we must compute the eigenvalues of the time evolution operator $\hat{U}$. But once the unit cell consists of two nonequivalent vertices, Fig. 8, the evolution within the unit cell requires two time steps. Thus, we need to consider the effective $\hat{U}_{\text{eff}}$ given by

$$\hat{U}_{\text{eff}} = \hat{U}^2, \tag{26}$$

so the eigenvalue equation reads

$$\hat{U}_{\text{eff}}\,|u\rangle = \exp[-2iE/\tilde{\varepsilon}]\,|u\rangle, \tag{27}$$

with E the eigenenergy associated to the eigenstate $|u\rangle$ and $\tilde{\varepsilon} = \hbar/\tau$.

As shown in Appendix A, $[\hat{U}_{\text{eff}}, \hat{T}_{\vec{R}_{(m_1,m_2)}}] = 0$. Nevertheless, although the effective time evolution and translation operators do commute, $|\sigma, \kappa_x, \kappa_y\rangle$, $|\sigma, \kappa_x, \kappa_y\rangle_{\text{even}}$, and $|\sigma, \kappa_x, \kappa_y\rangle_{\text{odd}}$, individually are not eigenstates of $\hat{U}_{\text{eff}}$ as a direct consequence of their degeneracy (see Appendix A). On the other hand, by writing

$$|u(\kappa_x,\kappa_y)\rangle = \sum_{\sigma=1}^{3} C_\sigma^{(+)}\,|\sigma,\kappa_x,\kappa_y\rangle_{\text{even}} + \sum_{\sigma=1}^{3} C_\sigma^{(-)}\,|\sigma,\kappa_x,\kappa_y\rangle_{\text{odd}} \tag{28}$$

in Appendix A, we prove that by properly choosing the $C_\sigma^{(+)}$ and $C_\sigma^{(-)}$ coefficients, the above $|u(\kappa_x,\kappa_y)\rangle$ solves Eq. (27). Moreover, the energy bands for the SQW in an infinite honeycomb lattice are obtained from

$$\det(\hat{F}\,\hat{\Gamma}^{(-)}\hat{F}^{\dagger}\,\hat{\Gamma}^{(+)} - \exp[-2iE/\tilde{\varepsilon}]\,\hat{\mathbf{1}}) = 0, \tag{29}$$

with the 3×3 diagonal matrix $\hat{F}$, function of κ_x and κ_y, having the non-null elements [see Eq. (A10)]

$$F_{\sigma\sigma} = \exp\left[i\,a\left(\frac{\sqrt{3}}{2}\,\kappa_x\,\sigma + \frac{3}{4}\,\kappa_y\,(-1)^\sigma\right)\right]. \tag{30}$$

The expression in Eq. (29) is rather elucidating. First, we observe that the elements of the matrix $\hat{F}$ depend straightforwardly on κ_x and κ_y, but they unequivocally encode all the hexagonal lattice topology information through the coefficients multiplying κ_x and κ_y. Actually, compare Eq. (30) with Eq. (1). Second, the site characteristics are fully determined by the 3×3 unitary matrices $\hat{\Gamma}^{(\pm)}$. We recall that in the present construction, generally we need two different matrices since we have two distinct sites in the unit cell (but see next section). Third, given the infinite many possibilities of setting $\hat{\Gamma}^{(\pm)} \in \mathrm{U}(3)$, this mathematically explains the huge diversity of the actual Dirac cone materials in 2D [12,76,77]. In fact, Eq. (29) generalizes recent important results pointing to further, i.e., beyond Dirac, geometric phase structures for 2D systems based on the group symmetry extension SU(2) → SU(3) [78] (see also Ref. [79]).

In the next section, we discuss a specific situation in which the energy bands $E(\kappa_x,\kappa_y)$ are analytically derived in a closed exact form. Concrete honeycomb lattice materials are addressed in Sec. VI.

V. AN EXACT SOLVABLE EXAMPLE: THE $\hat{\Gamma}_{AB}$ SCATTERING MATRIX

As previously emphasized, in the most general case for a honeycomb structure, we have two distinct scattering matrices, $\hat{\Gamma}^{(\pm)}$. Moreover, the corresponding $\hat{\Gamma}^{(\pm)}$ elements should reflect the eventually intricate interactions between the atoms forming the crystal. This will be more concretely illustrated in Sec. VI. However, we can get a proper qualitative understanding about the present approach by considering a simpler situation, namely, by setting $\hat{\Gamma}^{(+)} = \hat{\Gamma}^{(-)}$. Further, we can assume arbitrary, but fully symmetric $\hat{\Gamma}^{(+)} = \hat{\Gamma}^{(-)}$, thus allowing analytic computations.

So, next we suppose $\hat{\Gamma}^{(+)} = \hat{\Gamma}^{(-)} = \hat{\Gamma}_{AB}$, with $\hat{\Gamma}_{AB}$ in Eq. (14). Thus, we find from Eq. (29) that in such idealized model

$$0 = \left(\frac{|t_B(\theta)|^2}{4}h(\vec{\kappa}) - \cos^2[E/\tilde{\varepsilon}+\gamma]\right) \times (\sin[E/\tilde{\varepsilon}+\gamma-\theta] + 2\sin[E/\tilde{\varepsilon}+\gamma+\theta]), \tag{31}$$

with

$$h(\vec{\kappa}) = 3 + 4\cos\left[\frac{\sqrt{3}\kappa_x a}{2}\right]\cos\left[\frac{3\kappa_y a}{2}\right] + 2\cos[\sqrt{3}\kappa_x a], \tag{32}$$

where $0 \leqslant h(\vec{\kappa}) \leqslant 9$ for any κ_x, κ_y. Since the arguments of the sine functions in Eq. (31) do not depend on (κ_x,κ_y), the two $\vec{\kappa}$ dependent solutions of Eq. (31) read

$$E_\pm(\vec{\kappa},\theta,\gamma) = \tilde{\varepsilon}\left(\arccos\left[\mp\frac{|t_B(\theta)|}{2}\sqrt{h(\kappa_x,\kappa_y)}\right] - \gamma\right). \tag{33}$$

Equation (33) has three free parameters, γ, θ, and $\tilde{\varepsilon}$, which therefore can be arbitrarily set. For instance, γ is simply a global phase factor in the scattering matrix of Eq. (14). Nonetheless, from Eq. (33) we see that γ leads to a shift in the energy bands, thus constituting a tunable fitting parameter for the offset of the dispersion relations. Also, in the present particular case of $\hat{\Gamma}_{AB}$, if $\gamma = \pi/2$ then $|E_+(\vec{\kappa},\theta,\pi/2)| = |E_-(\vec{\kappa},\theta,\pi/2)|$.

Figure 10 displays plots of the energy bands from Eq. (33), normalized by $\tilde{\varepsilon}$, for various values of θ and $\gamma = \pi/2$. All of them exhibit the same symmetry regardless of the values of θ. The maximum values for E_+ and the minimum values for E_- are at the point Γ. The upper and lower bands touch each other at the K and K' points, corresponding to the hexagon vertices delimiting the first Brillouin zone, Fig. 9. There is a conical shape (Dirac cone) around K and K', i.e., the energy bands have a linear behavior as a function of the wave numbers around these high-symmetry points. This is akin to the graphene energy band structures [24].

Detailed density plots of the bands in Fig. 10—highlighting the first Brillouin zone—are depicted in Fig. 11. In particular, for $\theta = 0$ we recall that $\hat{\Gamma}_{AB}$ reduces to the Grover matrix, for which $|t_B(0)|^2 = 4/9$ assumes its maximum possible value. Analyzing the different graphs, we observe that $\theta = 0$ is the only situation where at point Γ (for which $\kappa_x = \kappa_y = 0$) the band does not display a smooth behavior. This fact is better visualized in Fig. 12, showing the band profiles along the direction connecting the points of high symmetry, namely, K, M, and Γ. Figure 12 also clearly illustrates that the bands touch each other at K and display the largest gap at Γ.

For $\gamma = \pi/2$ and arbitrary θ, the maximum of both $|E_+|$ and $|E_-|$ (at Γ) is given by

$$E_{\max}(\theta) = \tilde{\varepsilon}\left(\frac{\pi}{2} - \arccos\left[\frac{3}{2}|t_B(\theta)|\right]\right). \tag{34}$$

The variation of $E_{\max}$ with θ is displayed in Fig. 13. It vanishes for $|\theta|$ approaching $\pi/2$ once the transmission probability tends to zero for $\theta \to \pm\pi/2$ [cf. Eq. (15) and Fig. 2]. Such trend is easy to understand since for $\theta = \pi/2$, the SQW in the configuration space would become confined to the links occupied in the initial state.

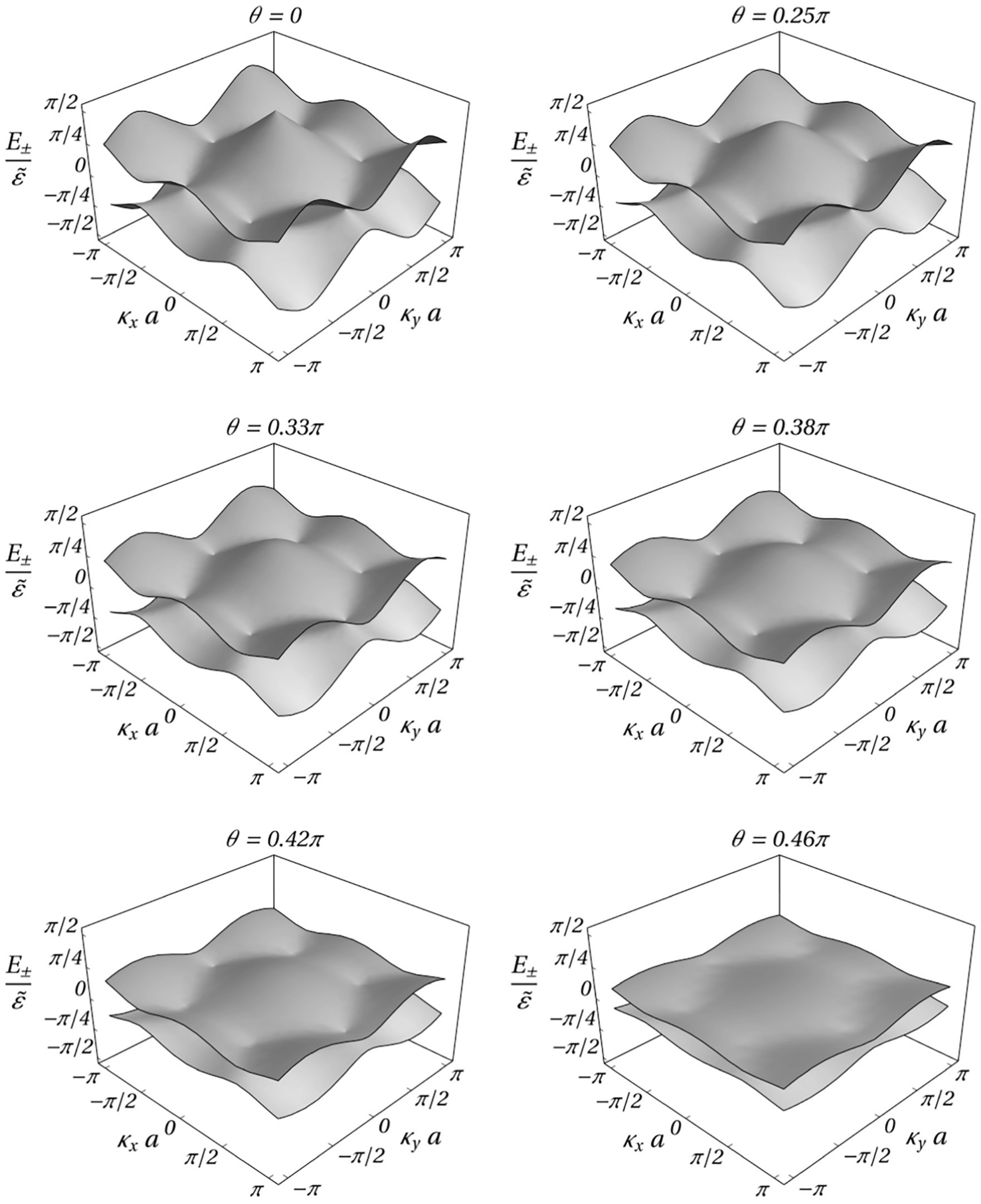

FIG. 10. For different values of θ and $\gamma = \pi/2$, the energy bands, divided by $\tilde{\varepsilon}$, resulting from Eq. (33).

A. The Fermi velocity and a tight-binding-like energy expression

As aforementioned, the energy bands in Eq. (33) display a linear behavior in the vicinity of K and K'. Hence, for $\gamma = \pi/2$ and defining

$$\vec{q} = \left(\kappa_x - \frac{2\pi}{3\sqrt{3}a}\right)\hat{e}_x + \left(\kappa_y - \frac{2\pi}{3a}\right)\hat{e}_y,$$

the expansion of Eq. (33) around K reads [for $\phi_q = \arctan[q_y/q_x]$ and $\vec{q} = (q_x, q_y)$]

$$E_\pm(\vec{q}, \theta, \pi/2) = \pm\frac{3\,\tilde{\varepsilon}\,|t_B(\theta)|}{4}\Bigg(a\,|\vec{q}| + \frac{\cos[3\,\phi_q]}{4}\,(a\,|\vec{q}|)^2 + \frac{(6\,|t_B(\theta)|^2 - \cos[6\,\phi_q] - 7)}{64}\,(a\,|\vec{q}|)^3 + \dots\Bigg). \tag{35}$$

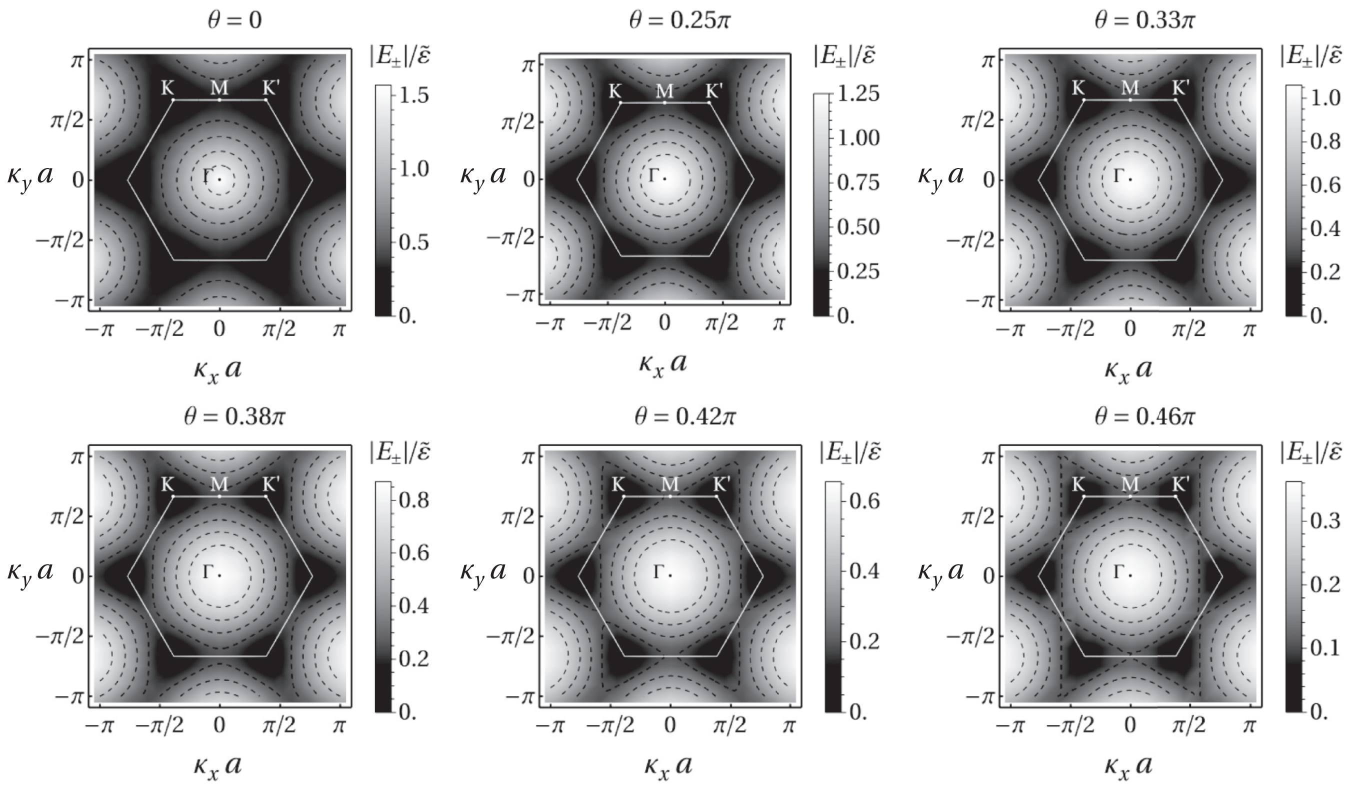

FIG. 11. For distinct θ's and $\gamma = \pi/2$, density plots of the modulus of the energy bands normalized by their maximum value (recall that in this case $|E_+| = |E_-|$). The hexagons represent the first Brillouin zone, with the high symmetry points Γ, M, K, and K' properly identified. The bands exhibit the same symmetry regardless of θ. The maximum for $|E_\pm|$ lies in the point Γ, moreover with $|E_\pm|$ tending to zero at the points K and K' (forming the Dirac cone).

Now, keeping only the linear term in $|\vec{q}|$, we have that in first order the energy bands around K can be written as a function of the Fermi velocity $\tilde{v}_F$ [24,81], or ($\vec{p} = \hbar\,\vec{q}$)

$$E_\pm(\vec{q},\theta,\pi/2) = \pm\tilde{v}_F(\theta)\,|\vec{p}|,$$
$$\tilde{v}_F(\theta) = \frac{3\,a\,\tilde{\varepsilon}\,|t_B(\theta)|}{4\,\hbar} = \frac{3\,a\,|t_B(\theta)|}{4\,\tau}. \tag{36}$$

Consistently, Eq. (36) corroborates the previous results for the MSD in Sec. II as well as the proposed Eq. (17), given that

$$K(\theta) = \frac{16}{9}\,\tilde{v}_F^2(\theta)\sum_{m=0}^{\infty} b_{2m}\,\cos^{2m}[\theta]. \tag{37}$$

In other words, the SQW MSD is proportional to the system Fermi velocity.

Furthermore, from Eq. (33) we can derive the group velocity through

$$\vec{v}_\pm(\vec{\kappa},\theta) = \frac{1}{\hbar}\nabla_{\vec{\kappa}}\,E_\pm(\vec{\kappa},\theta,\gamma). \tag{38}$$

Hence, for the system in the state represented by Eq. (28) and having the eigenvalues $E_\pm(\vec{\kappa},\theta,\gamma)$, we find

$$\vec{v}_\pm(\vec{\kappa},\theta) = \pm(v_x(\vec{\kappa},\theta)\,\hat{e}_x + v_y(\vec{\kappa},\theta)\,\hat{e}_y), \tag{39}$$

with

$$v_x(\vec{\kappa},\theta) = \frac{a\,\tilde{\varepsilon}}{\hbar}\frac{\sqrt{3}\,|\cos[\theta]|}{\sqrt{|5+4\cos[2\theta]|\,h(\vec{\kappa}) - (\cos[\theta]\,h(\vec{\kappa}))^2}} \times\left(2\cos\left[\frac{\sqrt{3}\kappa_x a}{2}\right]+\cos\left[\frac{3\kappa_y a}{2}\right]\right)\sin\left[\frac{\sqrt{3}\kappa_x a}{2}\right], \tag{40}$$

$$v_y(\vec{\kappa},\theta) = \frac{a\,\tilde{\varepsilon}}{\hbar}\frac{3\,|\cos[\theta]|}{\sqrt{|5+4\cos[2\theta]|\,h(\vec{\kappa}) - (\cos[\theta]\,h(\vec{\kappa}))^2}} \times\sin\left[\frac{3\kappa_y a}{2}\right]\cos\left[\frac{\sqrt{3}\kappa_x a}{2}\right]. \tag{41}$$

The group velocity is generally related to the scattering matrix reflection and transmission coefficients. As illustrations, notice first that $\vec{v}_\pm(\vec{\kappa},\theta \to \pi/2) \to 0$. But the reflection amplitude $|r_A(\theta)|$ in $\hat{\Gamma}_{AB}$ is maximum (and $t_B(\theta)$ is zero) exactly for $\theta = \pi/2$. Thus, the system becomes trapped, leading to a null group velocity. Second, it is not difficult to realize that $|\vec{v}_\pm(\vec{\kappa},\theta \to 0)| \to v_{max}(\kappa_x,\kappa_y)$. This is a consequence of $\theta = 0$ to yield the highest values for the transmission amplitude.

Lastly, regarding $\vec{v}_\pm(\vec{\kappa},\theta)$, from Eqs. (36) and (38) one easily finds that the modulus of the group velocity near the Dirac points coincides with the Fermi velocity expression.

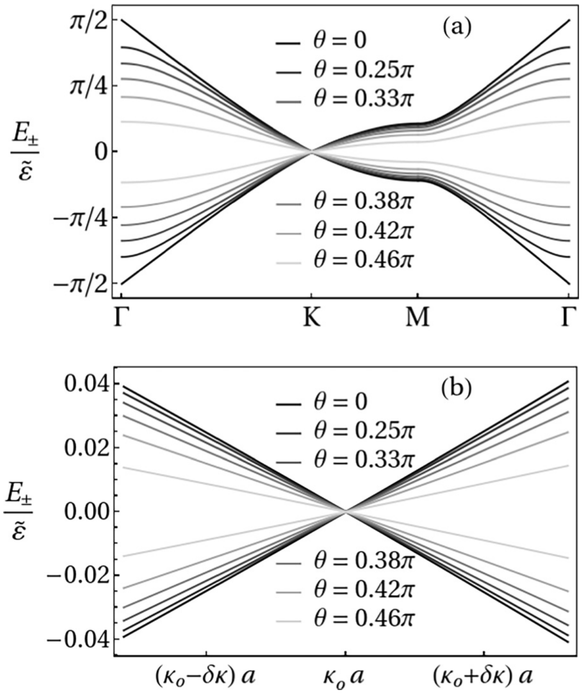

FIG. 12. (a) The energy band profiles, given by Eq. (33) with $\gamma = \pi/2$, in the direction connecting the points of high symmetry. (b) The linear behavior of the energy bands around the high-symmetry point K (and along the $\hat{e}_x$ direction). Here $\kappa_0\, a = 2\pi/(3\sqrt{3})$ and $\delta\kappa\, a = 0.05$.

We end this section deriving two relevant results in the literature, somewhat surprisingly given the simple assumptions made here, i.e., to set $\hat{\Gamma}^{(\pm)} = \hat{\Gamma}_{AB}$. Indeed, note that around the high-symmetry point K, $h(\kappa_x, \kappa_y)$ tends to zero. Then, from the series expansion

$$\arccos[x] = \frac{\pi}{2} - \sum_{n=0}^{\infty} \frac{(2n)!}{2^{2n}(n!)^2} \frac{x^{2n+1}}{2n+1}, \tag{42}$$

by taking $x = (\tilde{\varepsilon}\,|t_B(\theta)|/2)\sqrt{h(\kappa_x, \kappa_y)}$, in first order Eq. (33) simplifies to

$$E_\pm(\vec{\kappa}, \theta, \gamma) = \pm\varepsilon\sqrt{h(\kappa_x, \kappa_y)}, \tag{43}$$

where the hopping energy can be identified as

$$\varepsilon = \tilde{\varepsilon}\,|t_B(\theta)|/2. \tag{44}$$

Further, using Eq. (44), we can rewrite Eq. (36) as

$$\tilde{v}_F = \frac{3\,a\,\varepsilon}{2\hbar}. \tag{45}$$

Remarkably, Eq. (43) corresponds to the energy bands obtained from the tight-binding TB-1NN [80] model for the p_z orbital electrons of graphene [24,81]. In addition, Eq. (45) is completely akin to the expression relating the Fermi velocity to the hopping energy, as derived from the same TB-1NN approximation [24,81].

We shall point out that all the developments in this section—as to directly reproduce the tight-binding approximation and to derive Eq. (45)—are obtained by means of a very basic SQW model, grounded just on the pure topological structure of a honeycomb lattice and on a very symmetric local scattering matrix. These findings endorse the great significance of topology in establishing key properties of 2D materials. This will become even more evident from the analysis in the following section.

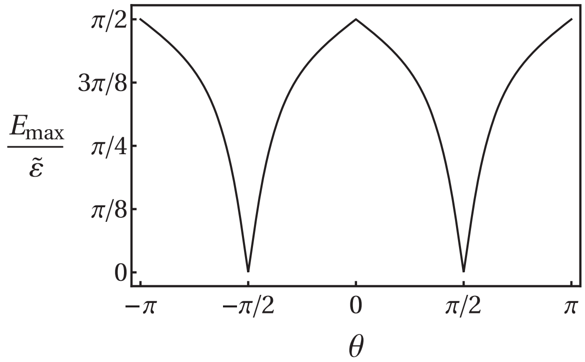

FIG. 13. $E_{\max}/\tilde{\varepsilon}$, Eq. (34), as function of θ.

VI. SQW AND ACTUAL 2D DIRAC MATERIALS

Having discussed the SQW theory for a general 2D hexagonal lattice structure, next we address concrete honeycomb bidimensional systems. With this aim, the graphene is certainly the natural candidate, being the most broadly studied Dirac material [21,22]. Nonetheless, two other important examples are germanene and silicene. Although both are not truly planar in a freestanding configuration, some studies have calculated their band energies assuming such a simplification (for proper discussions, see, e.g., Refs. [35–38,82,83]). We will suppose the same here.

We divide our analysis in two parts. We first consider the analytic expressions in Sec. V A, particularizing them to the above three materials. We then compare the results with computations in the literature. Second, we turn to the general Eq. (29). We demonstrate it can accurately capture the same profiles of the energy bands obtained via *ab initio* methods.

A. Energy bands from the scattering matrix $\hat{\Gamma}_{AB}$, Eq. (33)

1. Graphene

From the tight-binding model approximation TB-1NN [24,80] allied to some empirical considerations, the exchange energy between first-neighbor carbons in graphene has been estimated to be $\varepsilon \approx 2.75$ eV [24,84–86], whereas measurements lead to $\varepsilon \approx 3.0$ eV [24,87–90]. For their mutual distance, one finds $a = 1.42$ Å [81]. Hence, to contrast the energy bands via the SQW (under the simplified scheme in Sec. V A) with other approaches, we rewrite Eq. (44) as

$$\frac{\tilde{\varepsilon}\,|t_B(\theta)|}{2} = \varepsilon_{\text{eff}}. \tag{46}$$

So, ε_{eff} is an effective hopping energy associated to the bare parameters $\tilde{\varepsilon}$ and θ. For the graphene, we set ε_{eff} as either $\varepsilon_{\text{TB}} = 2.75$ eV or $\varepsilon_{\exp} = 3.0$ eV. For distinct θ, Table I displays the corresponding values of $\tilde{\varepsilon}$ and $\tau = \hbar/\tilde{\varepsilon}$ satisfying Eq. (46).

TABLE I. For graphene, assuming Eq. (46), the values of $\tilde{\varepsilon}$ and τ for distinct θ's.

θ	$\tilde{\varepsilon}$ (eV) for $\varepsilon_{\mathrm{TB}}$ (for $\varepsilon_{\mathrm{exp}}$)	τ (fs) for $\varepsilon_{\mathrm{TB}}$ (for $\varepsilon_{\mathrm{exp}}$)
0	08.3 (09.0)	0.0798 (0.0731)
$0.250\,\pi$	08.7 (09.5)	0.0756 (0.0694)
$0.333\,\pi$	09.5 (10.4)	0.0691 (0.0634)
$0.385\,\pi$	11.0 (12.0)	0.0598 (0.0548)
$0.420\,\pi$	13.5 (14.7)	0.0487 (0.0446)
$0.477\,\pi$	38.9 (42.4)	0.0169 (0.0155)

Different robust *ab initio* protocols aimed at investigating distinct aspects of graphene can be found in the literature (see, for example, Refs. [24,36,81,90–94]). In particular, for the energy bands, very reliable calculations are presented in Ref. [36] (hereafter *ab initio* 1) and in Ref. [94] (*ab initio* 2).

For six values of θ and $\varepsilon_{\mathrm{eff}} = \varepsilon_{\mathrm{TB}} = 2.75$ eV, in Fig. 14 we compare Eq. (33)—assuming $a = 1.42$ Å and the parameters in Table I—with the results from TB-NN1, *ab initio* 1, and *ab initio* 2 for the π and π^* graphene band structures. All the plots present the energy profiles along the direction of the high-symmetry points Γ, K, and M. As it should be (refer to Sec. V A), near the K point, regardless of θ, the energy bands from SQW and TB-1NN closely agree. On the other hand, around Γ the TB-NN1 approximation and Eq. (33) are similar only for $\theta \to \pi/2$. In fact, TB-NN1 and Eq. (33) coincide along the whole Γ–K–M curve just when $\theta \approx \pi/2$. Mathematically, this is so because then $|t_B(\theta \approx \pi/2)| \approx 0$ and a first-order truncation for the series in Eq. (42) works well for any value of the function $h(\kappa_x, \kappa_y)$.

Similarly to the TB-1NN approximation, Eq. (33) also yields upper and lower bands which are just specular images of each other (about $E = 0$). However, the plots from the *ab initio* approaches show that this is not the case, with the π and π^* bands displaying certain mutual asymmetries. Note that by varying θ, one can make Eq. (33) fairly agree with the *ab initio* methods either for the one or for the other band, but not for both simultaneously. This indicates that to suppose $\Gamma^{(+)} = \Gamma^{(-)}$ in Eq. (29) [as done to derive Eq. (33)] might be a too strong simplification for the energy bands calculations (see Sec. VI B).

As clear in Fig. 14, around the K point the tight-binding approximations and thus also Eq. (33) tend to coincide with more elaborated methods [84], like those from *ab initio* 1 and *ab initio* 2. Since the region in the vicinity of K is the foremost to determine transport features of graphene [81], the SQW framework in its simplest construction already constitutes a valuable tool to investigate the graphene transport characteristics.

Finally, in Fig. 15 we repeat the same plots of Fig. 14, but now with $\varepsilon_{\mathrm{eff}} = \varepsilon_{\mathrm{exp}} = 3.0$ eV. Qualitatively, the results are essentially the same as those in Fig. 14.

2. *Germanene and silicene*

Different works [36–38,82,83,99] discuss that the planar form of the germanene and silicene exhibit the same type of hybridization and lattice structure of graphene, but distinct lattice and hopping parameters. In this way, we can follow exactly the same previous SQW construction to also analyze these two 2D materials.

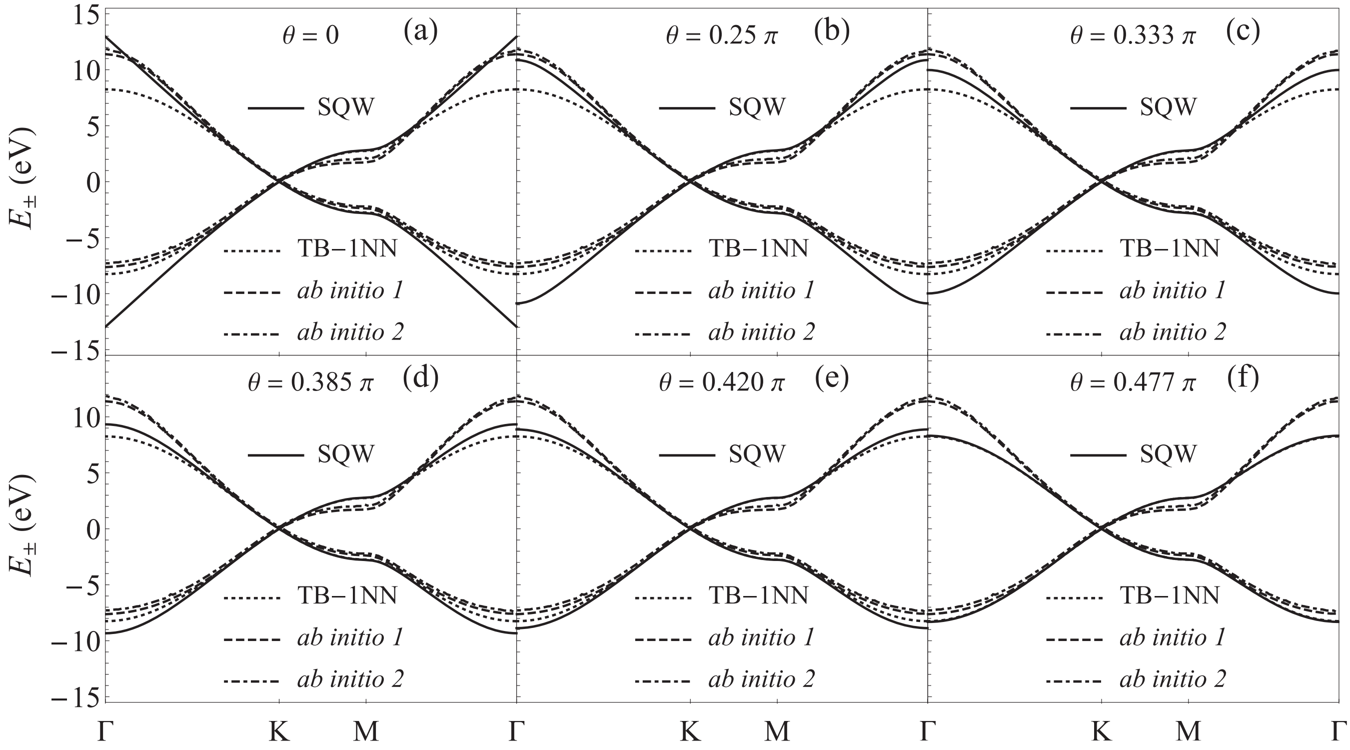

FIG. 14. Comparison between the graphene π and π^* energy band structures obtained via TB-1NN with $\varepsilon_{\mathrm{eff}} = \varepsilon_{\mathrm{TB}} = 2.75$ eV [Eq. (43)], *ab initio* 1 [36], *ab initio* 2 [94], and the SQW framework through Eq. (33), with $\gamma = \pi/2$ and six different values of θ. The *ab initio* curves have been digitalized from, respectively, Refs. [36,94].

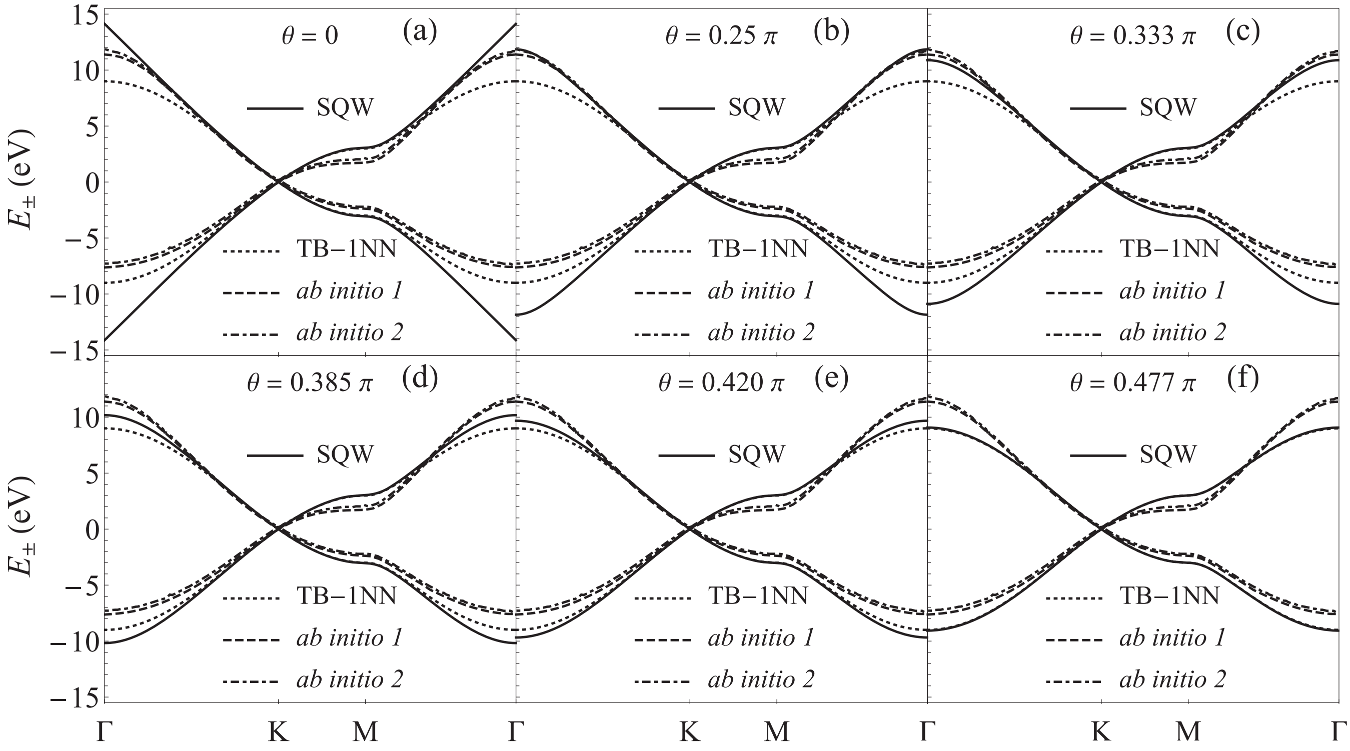

FIG. 15. The same as in Fig. 14, but for $\varepsilon_{\text{eff}} = \varepsilon_{\text{exp}} = 3.0$ eV.

Figures 16 and 17 depict, respectively, the planar germanene and silicene π and π^* energy bands. The plots compare the SQW, Eq. (33), for different θ values and $\gamma = \pi/2$, the TB-NN1 approximation, Eq. (43), and the *ab initio*

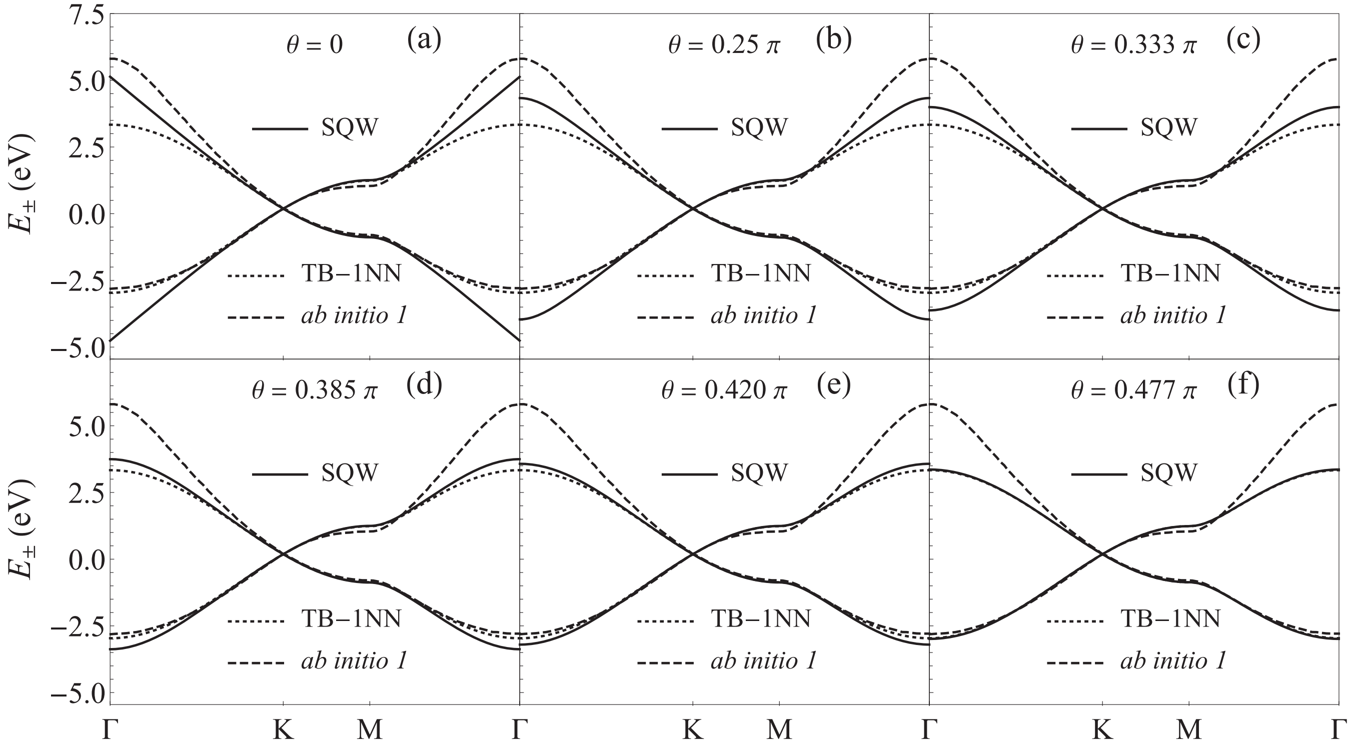

FIG. 16. Comparison between the planar germanene π and π^* band structures obtained via TB-1NN with $\varepsilon_{\text{eff}} = 1.05$ eV [Eq. (43)], *ab initio* 1 [36], and the SQW framework through Eq. (33), with $\gamma = \pi/2$ and six different values of θ. The *ab initio* 1 curve has been digitalized from Ref. [36].

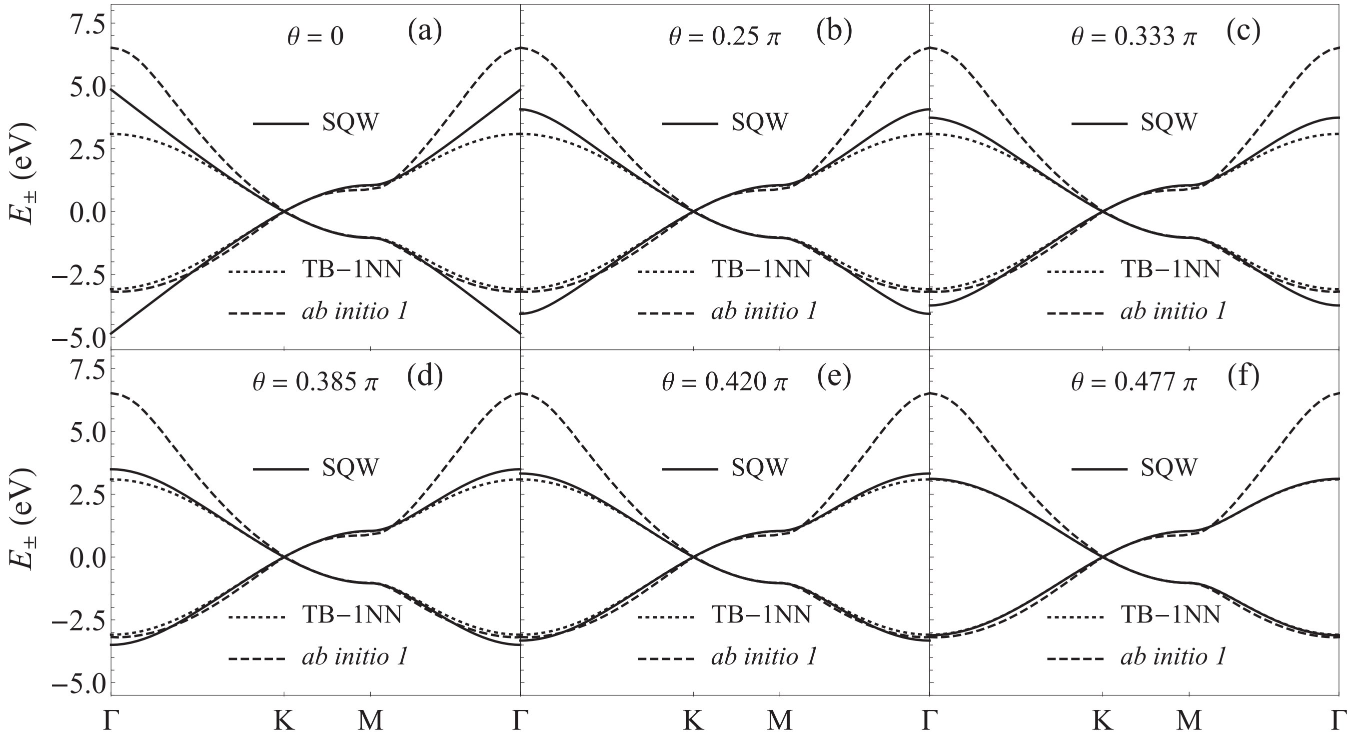

FIG. 17. Comparison between the planar silicene π and π^* band structures obtained via TB-1NN with $\varepsilon_{\text{eff}} = 1.03$ eV [Eq. (43)], *ab initio* 1 [36], and the SQW framework through Eq. (33), with $\gamma = \pi/2$ and six different values of θ. The *ab initio* 1 curve has been digitalized from Ref. [36].

1 of Ref. [36]. For a and ε_{eff}, refer to Table II. The overall trends of the SQW contrasted to the TB-1NN and *ab initio* 1 calculations are similar to those already observed for the graphene in Figs. 14 and 15. For instance, the SQW model gives very good results in the regions near the Dirac cones.

However, some distinctions can be identified. Taking the *ab initio* 1 curves as a reference, the upper (lower) bands of the germanene and silicene are better fitted by the SQW for smaller (larger) values of θ, a behavior akin to that found for graphene. But for the upper bands, the agreement is always greater for the graphene than for the germanene and silicene. Actually, for the latter two materials, the *ab initio* 1 upper band curves are always above those from the SQW for any θ. So, the Γ peaks in the graphene π^* band are fairly well described by SQW when $\theta \approx 0.25\pi$, which is not the case for germanene and silicene. On the other hand, around the M points of both bands, the SQW accordance tend to be higher in Figs. 16 and 17 than in Figs. 14 and 15.

TABLE II. Some parameters for the three 2D materials discussed in the present paper. For those resulting from the SQW model with the $\hat{\Gamma}_{AB}$ matrix, it has been set $\theta = \pi/3$ and $\gamma = \pi/2$.

Material	a (Å)[a]	ε_{eff}[b]	$v_F^{(\text{TB})}$[b]	$v_F^{(\text{SQW})}$[c]	$\tilde{\varepsilon}$	τ(fs)
Graphene	1.42	2.75	8.73	8.74	9.356	0.0704
Germanene	2.43	1.05	5.81	5.81	3.634	0.181
Silicene	2.28	1.03	5.35	5.35	3.567	0.185

[a] References [36,38,95].
[b] Hopping parameter (in eV) and Fermi velocity (in units of 10^5 m/s), for the TB-1NN model [36,96–98].
[c] Fermi velocity for the SQW via Eq. (36) (in units of 10^5 m/s).

3. Fermi velocity

Under the simplifying assumptions discussed in Sec. V A, the SQW model velocity near the Dirac cone regions is just the corresponding material Fermi velocity. It is given by the analytic approximation in Eq. (36).

By inspecting Figs. 14, 16, and 17, we see that $\theta = \pi/3$ leads to a good agreement between the SQW and the *ab initio* computations around the symmetry point K [see all the (c) panels] for the three discussed 2D materials.

Thus, considering Eqs. (36) and (46), with $\theta = \pi/3$, $\gamma = \pi/2$ and the corresponding materials parameters, we calculate $v_F^{(\text{SQW})}$. In Table II, we compare $v_F^{(\text{SQW})}$ with the tight-binding $v_F^{(\text{TB})}$ obtained in the literature [36,96–98]. As expected, the values are essentially the same, given the great agreement of SQW and TB-1NN around the symmetry point K.

B. Energy bands from the general expression in Eq. (29)

As we have seen in the particular case of hexagonal lattices, topology is one of the most relevant characteristics of SQW models, where the dynamics is fully specified by the scattering matrices and the spatial evolution established by the periodic lattice local connectivity. Such key traits are manifested in the very general expression for the energy bands in Eq. (29). For instance, the former (latter) factor is concretely taken into account by $\hat{\Gamma}^{(\pm)}$ ($\hat{F}$) in Eq. (29). Therefore, if a formula like Eq. (29) can accurately lead to the actual energy bands of 2D

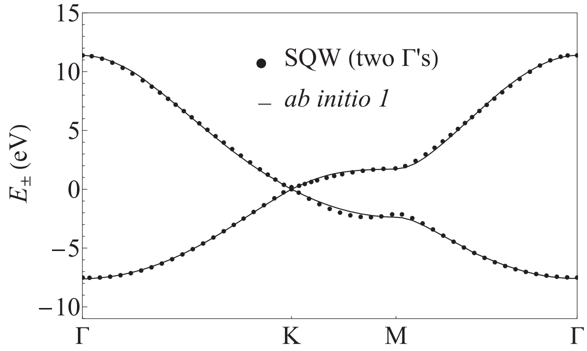

FIG. 18. The graphene energy band structures from Eq. (29), with $\Gamma^{(+)} \neq \Gamma^{(-)}$ (see main text). The results are compared with those from the *ab initio* 1 method [36].

honeycomb systems, this certainly must be regarded as further and very compelling evidence that important properties of 2D materials are indeed driven, at least in part [64], by their topological features.

From the particular choice $\hat{\Gamma}^{(\pm)} = \hat{\Gamma}_{AB}$ in Sec. V, we have been able to improve the traditional tight-binding approximation; refer to Eqs. (33), (35), and (36). However, Eq. (33) does not yield an overall good description for the π and π^* bands when compared to more precise calculations from *ab initio* methods (often employing DFT together with parametrization schemes, where relevant parameters are empirically or semiempirically estimated). One problem is that $\hat{\Gamma}_{AB}$ is somewhat limited, depending only on two parameters, one a global phase. So, conceivably it cannot properly capture all the local physical-chemical aspects (e.g., the molecular orbital features) of concrete materials as graphene.

Given the above, a key question is whether or not there are $\hat{\Gamma}^{(\pm)}$'s such that Eq. (29) can properly describe the energy bands $E_\pm(\kappa_x, \kappa_y)$ of a 2D honeycomb material. To address this, the purpose next is not to compute $\hat{\Gamma}^{(\pm)}$ from first principles, say, from molecular orbitals calculations (nonetheless, see the remarks in Sec. VII). Instead, we shall numerically verify if specific $\hat{\Gamma}^{(\pm)}$ into Eq. (29) can reproduce the results from the much more elaborated and involved *ab initio* approaches.

Thus, we have first written our U(3) matrices $\hat{\Gamma}^{(\pm)}$ in terms of a general parametrization proposed in Ref. [100] (details in Appendix B). Then, we have numerically varied these parameters, generating distinct $\hat{\Gamma}^{(\pm)}$'s. By solving the corresponding Eq. (29), we have compared the obtained energy bands with those from *ab initio* 1 [36], selecting the best results. The full computational algorithm is described in Appendix C.

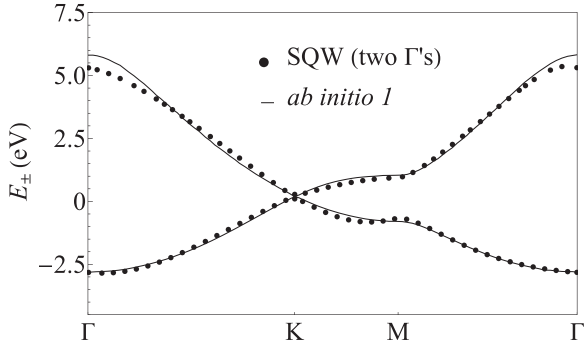

FIG. 19. The same than in Fig. 18, but for the planar germanene.

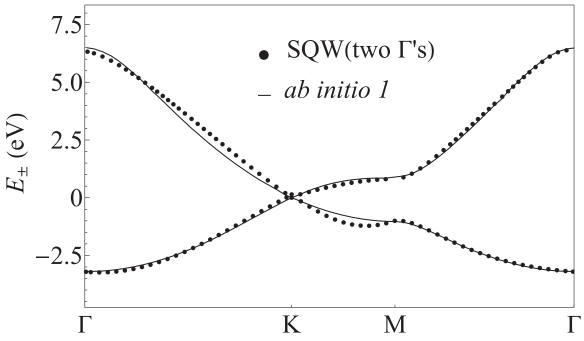

FIG. 20. The same than in Fig. 18, but for the planar silicene.

We have analyzed two situations. The first taking $\hat{\Gamma}^{(+)} = \hat{\Gamma}^{(-)} = \hat{\Gamma}$. We observe this instance is computationally reasonably fast to run. Then, an extensive scan in the parameters space of $\hat{\Gamma}$ was possible. As they should, the energy profiles obtained (not shown) are better than those from Eq. (33) in Sec. VI A. Nevertheless, we have found that if one band is globally very similar to *ab initio* 1, the other, although overall displaying a fair agreement, still presents some relevant discrepancies in certain (κ_x, κ_y) intervals.

The second, obviously computationally more time consuming, has been to assume $\hat{\Gamma}^{(+)}$ and $\hat{\Gamma}^{(-)}$ arbitrary. In this case, by running the algorithm in Appendix C in a simple personal computer of processor i7-9750h (4 Mhz) and 16 GB of RAM, for each system studied we have tested about 500 000 pairs of matrices for a simulation time of approximately 60 min. The best matrices found are those in Eq. (B3), Appendix B. The corresponding energy band structures are displayed in Figs. 18–20, respectively, for graphene, germanene, and silicene.

We note that distinctly from the previous section, for the graphene in Fig. 18 we see a global high similarity between the curves from Eq. (29) and from the *ab initio* 1 protocol. A certain discrepancy can be identified along the region between the symmetry points K–M, more sensibly for the lower band. But even then, the accordance is still fine.

For the germanene, Fig. 19, and silicene, Fig. 20, overall the agreement is satisfactory, although not as good as for the graphene. For example, observe in Fig. 19 that there are some deviations, with Eq. (29) resulting in lower energy values for the upper band close to the Γ symmetry points. In Fig. 20, the discrepancies are observed in different regions, along Γ–K for the upper band and along K–M for the lower band.

We finally mention that the greater concurrence of the SQW model with graphene than with germanene and silicene is probably related to a fundamental geometrical feature of the latter two materials. They are, in fact, buckled structures, not fully stabilizing in the planar form [35,36,42,99,101] if not deposited on substrates, like gold [102]. The buckling is known to alter the band gap and shapes (from the eventual flat disposition) in certain (κ_x, κ_y) ranges. Thus, aimed to a perfect planar arrangement, our present framework might not fully describe the actual bands profiles of these materials in their innate bent configurations. Furthermore, some assumptions made in typical *ab initio* calculations for germane and silicene, being ways to mitigate their nonplanarity [35,101,103–106], introduce few deviations from the correct bands. In this way, some mismatches observed in Figs. 19 and 20 may also be artifacts arising from such approximations.

VII. FINAL REMARKS AND CONCLUSION

Motivated by the importance of topology in setting distinct properties of 2D materials, we have developed a SQW model to study honeycomb lattice systems. In such a framework, local scattering dynamics are determined by arbitrary 3×3 unitary matrices $\hat{\Gamma}$, defined on the network distinct sites. The crystal case is established by supposing just two matrices $\hat{\Gamma}^{(\pm)}$ for the whole infinite structure, associated to the two sites of the Wigner-Seitz cell.

For the simpler case of $\hat{\Gamma}^{(+)} = \hat{\Gamma}^{(-)} = \hat{\Gamma}_{AB}(\theta, \gamma)$, with $\hat{\Gamma}_{AB}$ given in Eq. (14), we have analyzed time evolution in the configuration space, discussing characteristics as the associated MSD and probability distributions along the lattice bonds. As usual in QW models—and similarly to actual suspended graphene structures [107]—we have observed ballisticlike transport behavior in the system.

Formulating the problem in the momentum space, we have derived a rather general expression, Eq. (29), yielding the model energy bands as function of the scattering matrices $\hat{\Gamma}^{(\pm)}$. Again assuming $\hat{\Gamma}^{(\pm)} = \hat{\Gamma}_{AB}(\theta, \gamma)$, the energy profiles $E_{\pm}(\vec{\kappa}, \theta, \gamma)$ are then given by Eq. (33). From Eq. (33) we have straightforwardly derived the same tight-binding TB-1NN energies, group velocity, and Fermi velocity formulas known in the literature (see, e.g., Refs. [24,81]). By varying θ and γ, the energy bands in Eq. (33) have been compared with accurate *ab initio* calculations for the paradigmatic graphene (a honeycomb Dirac material) as well as for two important 2D crystals, germanene and silicene. Although the energy curves can be made very similar in different relatively large regions of (κ_x, κ_y) and are consistently better than the tight-binding approximation, an everywhere (in $\vec{\kappa}$) good agreement using an unique pair of values for (θ, γ) is not possible.

Lastly, by exploring the general Eq. (29)—i.e., allowing $\hat{\Gamma}^{(+)}$ and $\hat{\Gamma}^{(-)}$ to be arbitrary—we have demonstrated that by means of appropriate numerical choices for such matrices, the agreement between our simple calculations with *ab initio* methods is very good for graphene and rather satisfactory for germanene and silicene. The discrepancies for these two last examples are likely connected to the fact they are not really stable in a full planar form. We also mention that for germanene and silicene, although a small effect, spin-orbit coupling (not included in the *ab initio* schemes considered here) can induce a small opening of the Dirac point [106]. Interestingly, this effect may be incorporated into our formalism through the matrices $\hat{\Gamma}^{(\pm)}$. This will be the subject of a forthcoming contribution.

Our present findings naturally raise a few relevant questions. From a fundamental point of view, a crucial one relates to the exactness of Eq. (29). In Sec. VI B, we have seen our construction does lead to fine numerical results. Nonetheless, a key issue is if the energy bands of a honeycomb 2D crystal can indeed be exactly described by the expression in Eq. (29)—of course, provided $\hat{\Gamma}^{(\pm)}$ are correctly specified. Some facts seem to point to a positive answer. First, it has been rigorously proved for a hexagonal lattice [108] that local scattering matrices, our $\hat{\Gamma}^{(\pm)}$, should completely determine any symmetric compact support potential (so, the typical atomic interactions forming localized orbitals [109]) along a bond—see also Ref. [110]. This complies with certain scattering methods able to unveil properties of molecular orbitals in molecular crystals [111] and the spatial shapes of orbitals in molecules [112]. Second, the functional form of Eq. (29), demanding only two scattering matrices for the two nonequivalent sites in the basic cell (Sec. IV), are in complete accordance with *ab initio* approaches, mainly constructed from the potentials between the atoms in the basic cell [24,25,104].

Conversely, from a practical perspective the important point is how to adequately determine the scattering matrices. We emphasize that in this paper, instead of calculating $\hat{\Gamma}^{(\pm)}$ from first principles, our goal has been to show that their proper choice in Eq. (29) does result in the energy bands of representative 2D crystal materials (graphene, germane, and silicene). Therefore, we have numerically searched for $\hat{\Gamma}^{(\pm)}$ so as to reproduce accurate results in the literature. However, for novel systems obviously one would need to obtain $\hat{\Gamma}^{(\pm)}$ by means of independent procedures (for a useful parallel in the context of photonic crystals see, e.g., Refs. [58,113]). A possible scheme would be to define an artificial molecule-constituted by the (eventually extended) lattice primitive cell and from *ab initio* quantum chemistry protocols, allied to QW models [54,55] to solve for the molecular orbitals and thus to obtain $\hat{\Gamma}^{(\pm)}$ from the orbitals overlaps (e.g., following the prescription mentioned in Ref. [112]). Currently, this is under investigation and progress will be reported in due course.

As a final potential application, we recall we have addressed perfect infinite crystals. But our approach could easily be considered for finite honeycomb sheets. In such context, SQW models would be particularly useful to test finite size effects [114], e.g., how the geometry of specific boundary conditions, such as zigzag, armchair and even their combination, would determine the conductivity character of nanoribbons.

ACKNOWLEDGMENTS

H.S.G. would like to thank CAPES for a PhD fellowship. M.G.E.L. acknowledges research grants from Conselho Nacional de Desenvolvimento Cientfico e Tecnológico (CNPq) (Grant No. 304532/2019-3) and from the project "Efficiency in uptake, production and distribution of photovoltaic energy distribution as well as other sources of renewable energy sources" (Grant No. 88881.311780/2018-00) via CAPES PRINT-UFPR.

APPENDIX A: THE ACTION OF $\hat{U}_{\text{eff}}$ ON THE MOMENT EIGENSTATES AND THE ENERGY BANDS DERIVATION

Here we derive important results for Sec. IV. We start by showing that $[\hat{U}_{\text{eff}}, \hat{T}_{\vec{R}_{(m_1,m_2)}}] = 0$.

Given $|\sigma, j, k\rangle$ in Eq. (24), $\vec{r}_{(j,k)} = (x_j, y_k)$ in Eq. (1), and the relation in Eq. (22), we have

$$\hat{T}_{\vec{R}_{(m_1,m_2)}} |\sigma, j, k\rangle = |\sigma, j + m_1 - m_2, k + 2\,(m_1 + m_2)\rangle. \quad \text{(A1)}$$

With the help of Eq. (4), we can write $\hat{U}$ in the basis $\{|\sigma, j, k\rangle\}$ as

$$\hat{U} = \sum_{j,k} \sum_{\sigma} \sum_{\sigma'} \Gamma^{((-1)^k)}_{\sigma'\sigma} |\sigma', \mathcal{J}(\sigma', j, k), \mathcal{K}(\sigma', j, k)\rangle \langle \sigma, j, k|. \quad \text{(A2)}$$

Then, from Eqs. (A1), (20), and (21):

$$\hat{T}_{\vec{R}_{(m_1,m_2)}} \hat{U} = \sum_{j,k} \sum_{\sigma} \sum_{\sigma'} \Gamma^{((-1)^k)}_{\sigma'\sigma} |\sigma', \mathcal{J}(\sigma', j, k) + m_1 - m_2, \mathcal{K}(\sigma', j, k) + 2\,(m_1 + m_2)\rangle \langle \sigma, j, k|, \quad \text{(A3)}$$

$$\hat{U}\, \hat{T}_{\vec{R}_{(m_1,m_2)}} = \sum_{j,k} \sum_{\sigma} \sum_{\sigma'} \Gamma^{((-1)^k)}_{\sigma'\sigma} |\sigma', \mathcal{J}(\sigma', j, k), \mathcal{K}(\sigma', j, k)\rangle \langle \sigma, j - m_1 + m_2, k - 2\,(m_1 + m_2)|. \quad \text{(A4)}$$

Now, from the labeling change $j \to j - m_1 + m_2$ and $k \to k - 2\,(m_1 + m_2)$ in Eq. (A4) and since

$$\begin{aligned} \mathcal{J}(\sigma, j + m_1 - m_2, k + 2\,(m_1 + m_2)) &= \mathcal{J}(\sigma, j, k) + m_1 - m_2, \\ \mathcal{K}(\sigma, j + m_1 - m_2, k + 2\,(m_1 + m_2)) &= \mathcal{K}(\sigma, j, k) + 2\,(m_1 + m_2), \end{aligned} \quad \text{(A5)}$$

one readily finds that Eqs. (A3) and (A4) coincide. So, the commutation between $\hat{U}$ and $\hat{T}$ is established and, consequently, that between $\hat{U}_{\text{eff}} = \hat{U}^2$ and $\hat{T}$.

Next we address the action of $\hat{U}_{\text{eff}}$ (representing two time steps) on the momentum states of Eq. (24). Observe that if k is even (odd) then $\mathcal{K}(\sigma, j, k)$ is odd (even) regardless of σ and j. Thus, from Eqs. (4) and (5), it reads

$$\begin{aligned} \hat{U}_{\text{eff}}\, |\sigma, j, k\rangle &= \sum_{\sigma'} \sum_{\sigma''} \Gamma^{((-1)^k)}_{\sigma'\sigma}\, \Gamma^{(-(-1)^k)}_{\sigma''\sigma'}\, |\sigma'', \mathcal{J}(\sigma'', \mathcal{J}(\sigma', j, k), \mathcal{K}(\sigma', j, k)), \mathcal{K}(\sigma'', \mathcal{J}(\sigma', j, k), \mathcal{K}(\sigma', j, k))\rangle, \\ &= \sum_{\sigma'} \sum_{\sigma''} \Gamma^{((-1)^k)}_{\sigma'\sigma}\, \Gamma^{(-(-1)^k)}_{\sigma''\sigma'}\, |\sigma'', j + (-1)^k\,(\sigma' - \sigma''), k + (-1)^k\,((-1)^{\sigma'} - (-1)^{\sigma''})\rangle. \end{aligned} \quad \text{(A6)}$$

We shall write the above equation in the momentum space. With this goal, we consider Eq. (24), also setting $f(\sigma'', \sigma') = (\sigma' - \sigma'')$ and $g(\sigma'', \sigma') = (-1)^{\sigma'} - (-1)^{\sigma''}$. Hence

$$\begin{aligned} \hat{U}_{\text{eff}}\, |\sigma, \kappa_x, \kappa_y\rangle = \frac{1}{\mathcal{N}} \sum_{j} \sum_{k} \sum_{\sigma''} \sum_{\sigma'} &\Gamma^{((-1)^k)}_{\sigma'\sigma}\, \Gamma^{(-(-1)^k)}_{\sigma''\sigma'}\, \exp[i\,(\kappa_x\, x_j + \kappa_y\, y_k)] \\ &\times |\sigma'', j + (-1)^k\, f(\sigma'', \sigma'), k + (-1)^k\, g(\sigma'', \sigma')\rangle. \end{aligned} \quad \text{(A7)}$$

Under $\hat{U}_{\text{eff}}$, a state corresponding to site (j, k) can evolve only to the states associated to sites (j', k') belonging to the set

$$(j', k') \in \{(j, k), (j \pm 2, k), (j \pm 1, k - 2), (j \pm 1, k + 2)\}.$$

In this way, k and k' have the same parity. Also, from Eq. (1)

$$\begin{aligned} x_{(j' - (-1)^{k'}\, f(\sigma'', \sigma'))} &= x_{j'} - (-1)^{k'}\, \frac{\sqrt{3}}{2}\, f(\sigma'', \sigma')\, a, \\ y_{(k' - (-1)^{k'}\, g(\sigma'', \sigma'))} &= y_{k'} - (-1)^{k'}\, \frac{3}{4}\, g(\sigma'', \sigma')\, a. \end{aligned} \quad \text{(A8)}$$

Then, from the following changes in Eq. (A7): $j' = j + (-1)^k\, f(\sigma'', \sigma')$ and $k' = k + (-1)^k\, g(\sigma'', \sigma')$, we get

$$\begin{aligned} \hat{U}_{\text{eff}}\, |\sigma, \kappa_x, \kappa_y\rangle &= \frac{1}{\mathcal{N}} \sum_{j'} \sum_{k'} \sum_{\sigma''} \sum_{\sigma'} \Gamma^{[-(-1)^{k'}]}_{\sigma''\sigma'} \Gamma^{[(-1)^{k'}]}_{\sigma'\sigma}\, \exp\left[-\, i\, (-1)^{k'}\, a \left(\frac{\sqrt{3}}{2}\, f(\sigma'', \sigma')\, \kappa_x + \frac{3}{4}\, g(\sigma'', \sigma')\, \kappa_y \right) \right] \\ &\quad \times \exp[i\,(\kappa_x\, x_{j'} + \kappa_y\, y_{k'})]\, |\sigma'', j', k'\rangle \\ &= \frac{1}{\mathcal{N}} \sum_{\sigma''} \sum_{\sigma'} \Bigg\{ \sum_{j'} \sum_{k'_{\text{even}}} \Gamma^{(-)}_{\sigma''\sigma'} \Gamma^{(+)}_{\sigma'\sigma}\, \exp\left[-\, i\, a \left(\frac{\sqrt{3}}{2}\, (\sigma' - \sigma'')\, \kappa_x + \frac{3}{4}\, [(-1)^{\sigma'} - (-1)^{\sigma''}]\, \kappa_y \right) \right] \\ &\quad + \sum_{j'} \sum_{k'_{\text{odd}}} \Gamma^{(+)}_{\sigma''\sigma'}\, \Gamma^{(-)}_{\sigma'\sigma}\, \exp\left[+\, i\, a \left(\frac{\sqrt{3}}{2}\, (\sigma' - \sigma'')\, \kappa_x + \frac{3}{4}\, [(-1)^{\sigma'} - (-1)^{\sigma''}]\, \kappa_y \right) \right] \Bigg\} \end{aligned}$$

$$\times\, \exp[i\,(\kappa_x\, x_{j'} + \kappa_y\, y_{k'})]\, |\sigma'', j', k'\rangle.$$

$$= \sum_{\sigma''} (\hat{F}\, \hat{\Gamma}^{(-)} \hat{F}^{\dagger}\, \hat{\Gamma}^{(+)})_{\sigma''\sigma}\, |\sigma'', \kappa_x, \kappa_y\rangle_{\text{even}} + \sum_{\sigma''} (\hat{F}^{\dagger}\, \hat{\Gamma}^{(+)} \hat{F}\, \hat{\Gamma}^{(-)})_{\sigma''\sigma}\, |\sigma'', \kappa_x, \kappa_y\rangle_{\text{odd}}. \tag{A9}$$

Above, the diagonal unitary matrix $\hat{F}$ has the elements (for $\delta_{\sigma''\sigma'}$ the usual Kronecker's delta)

$$F_{\sigma''\sigma'} = \exp\left[i\, a \left(\frac{\sqrt{3}}{2}\, \kappa_x\, \sigma'' + \frac{3}{4}\, \kappa_y\, (-1)^{\sigma''} \right) \right] \delta_{\sigma''\sigma'}. \tag{A10}$$

From the actual structure of Eq. (A9), one directly sees that neither $|\sigma, \kappa_x, \kappa_y\rangle$, $|\sigma, \kappa_x, \kappa_y\rangle_{\text{even}}$ or $|\sigma, \kappa_x, \kappa_y\rangle_{\text{odd}}$ are eigenstates of $\hat{U}_{\text{eff}}$. But then we consider

$$|u(\kappa_x, \kappa_y)\rangle = \sum_{\sigma} C_{\sigma}^{(+)}\, |\sigma, \kappa_x, \kappa_y\rangle_{\text{even}} + \sum_{\sigma} C_{\sigma}^{(-)}\, |\sigma, \kappa_x, \kappa_y\rangle_{\text{odd}}. \tag{A11}$$

By imposing that

$$\hat{U}_{\text{eff}}\, |u(\kappa_x, \kappa_y)\rangle = \exp[-2iE/\tilde{\varepsilon}]\, |u(\kappa_x, \kappa_y)\rangle, \tag{A12}$$

it reads [for $\hat{O}$ a 3 × 3 null matrix and for $s = \pm$ with $C^{(s)^{\text{T}}} = (C_1^{(s)}\, C_2^{(s)}\, C_3^{(s)})$]

$$\begin{pmatrix} \hat{F}\, \hat{\Gamma}^{(-)} \hat{F}^{\dagger}\, \hat{\Gamma}^{(+)} & \hat{O} \\ \hat{O} & \hat{F}^{\dagger}\, \hat{\Gamma}^{(+)} \hat{F}\, \hat{\Gamma}^{(-)} \end{pmatrix} \begin{pmatrix} C^{(+)} \\ C^{(-)} \end{pmatrix} = \exp[-2iE/\tilde{\varepsilon}] \begin{pmatrix} C^{(+)} \\ C^{(-)} \end{pmatrix}. \tag{A13}$$

The solution of Eq. (A13) implies that (with $\hat{\mathbf{1}}$ the 3 × 3 identity matrix)

$$0 = \det\big(\hat{F}\, \hat{\Gamma}^{(-)} \hat{F}^{\dagger}\, \hat{\Gamma}^{(+)} - \exp[-2iE/\tilde{\varepsilon}]\, \hat{\mathbf{1}}\big)\, \det(\hat{F}^{\dagger}\, \hat{\Gamma}^{(+)} \hat{F}\, \hat{\Gamma}^{(-)} - \exp[-2iE/\tilde{\varepsilon}]\, \hat{\mathbf{1}}). \tag{A14}$$

It is straightforward to prove that both determinants in Eq. (A14) result in the same expression. So, the energy bands for our problem is given by Eq. (29) in Sec. IV.

APPENDIX B: A GENERAL PARAMETRIZATION FOR THE UNITARY MATRICES $\hat{\Gamma}^{(\pm)}$

To search for appropriate scattering matrices in Eq. (29), leading to numerically accurate energy bands, it is very handy to consider a specific parametrization for $\hat{\Gamma}^{(\pm)}$. Therefore, we adopt the one proposed in Ref. [100]. Supposing the same global phase factor $\gamma^{(+)} = \gamma^{(-)} = \gamma$, we write $\hat{\Gamma}^{(\pm)} = \exp[i\,\gamma]\, \hat{S}^{(\pm)}$, so the SU(3) matrices $\hat{S}$ are written as

$$\hat{S} = \begin{pmatrix} S_{11} & S_{12} & S_{13} \\ S_{21} & S_{22} & S_{23} \\ S_{31} & S_{32} & S_{33} \end{pmatrix}, \tag{B1}$$

where [100]

$$\begin{aligned}
&S_{11} = \cos[\theta_1]\, \cos[\theta_2]\, \exp[i\,\phi_1], \quad S_{22} = \cos[\theta_1]\, \cos[\theta_3]\, \exp[i\,\phi_2], \\
&S_{33} = \cos[\theta_2]\, \cos[\theta_3]\, \exp[-i\,(\phi_1 + \phi_2)] - \sin[\theta_1]\, \sin[\theta_2]\, \sin[\theta_3]\, \exp[i\,(-\phi_3 + \phi_4 + \phi_5)], \\
&S_{21} = \sin[\theta_2]\, \sin[\theta_3]\, \exp[-i\,(\phi_4 + \phi_5)] - \sin[\theta_1]\, \cos[\theta_2]\, \cos[\theta_3]\, \exp[i\,(\phi_1 + \phi_2 - \phi_3)],\ S_{12} = \sin[\theta_1]\, \exp[i\,\phi_3], \\
&S_{23} = -\cos[\theta_2]\, \sin[\theta_3]\, \exp[-i(\phi_1 + \phi_5)] - \sin[\theta_1]\, \sin[\theta_2]\, \cos[\theta_3]\, \exp[i\,(\phi_2 - \phi_3 + \phi_4)],\ S_{32} = \cos[\theta_1]\, \sin[\theta_3]\, \exp[i\,\phi_5], \\
&S_{31} = -\sin[\theta_1]\, \cos[\theta_2]\, \sin[\theta_3]\, \exp[i\,(\phi_1 - \phi_3 + \phi_5)] - \sin[\theta_2]\, \cos[\theta_3]\, \exp[-i\,(\phi_2 + \phi_4)],\ S_{13} = \cos[\theta_1]\, \sin[\theta_2]\, \exp[i\,\phi_4].
\end{aligned} \tag{B2}$$

Here $0 \leqslant \theta_1, \theta_2, \theta_3 \leqslant \pi/2$, $0 \leqslant\ \phi_1, \phi_2, \phi_3, \phi_4, \phi_5 \leqslant 2\pi$.

Then, we have numerically varied the parameters as defined above (both for $\hat{\Gamma}^{(+)}$ and $\hat{\Gamma}^{(-)}$), solved the corresponding Eq. (29), and compared the obtained energy bands with the computations from the *ab inition* methods mentioned in the main text, looking for the best agreements. From such (limited in time) searching procedure, see Appendix C, we have found that the optimal $\hat{S}^{(\pm)}$'s are

$$\hat{S}^{(+)}_{\text{graf}} = \begin{pmatrix} -0.688114 - 0.150771\,i & -0.246765 - 0.2626\,i & -0.381596 - 0.477807\,i \\ -0.180346 + 0.405402\,i & -0.410796 - 0.418278\,i & 0.67699 + 0.0331718\,i \\ -0.546443 + 0.0910583\,i & 0.317197 + 0.652552\,i & 0.399643 - 0.0834001\,i \end{pmatrix},$$

$$\hat{S}^{(-)}_{\text{graf}} = \begin{pmatrix} -0.138184 + 0.00919204\,i & -0.828744 + 0.438194\,i & -0.315014 + 0.0525038\,i \\ 0.867777 + 0.0560679\,i & 0.0422888 + 0.0754977\,i & -0.424689 - 0.236579\,i \\ 0.20242 + 0.428562\,i & -0.124223 - 0.313448\,i & -0.0501766 + 0.811888\,i \end{pmatrix},$$

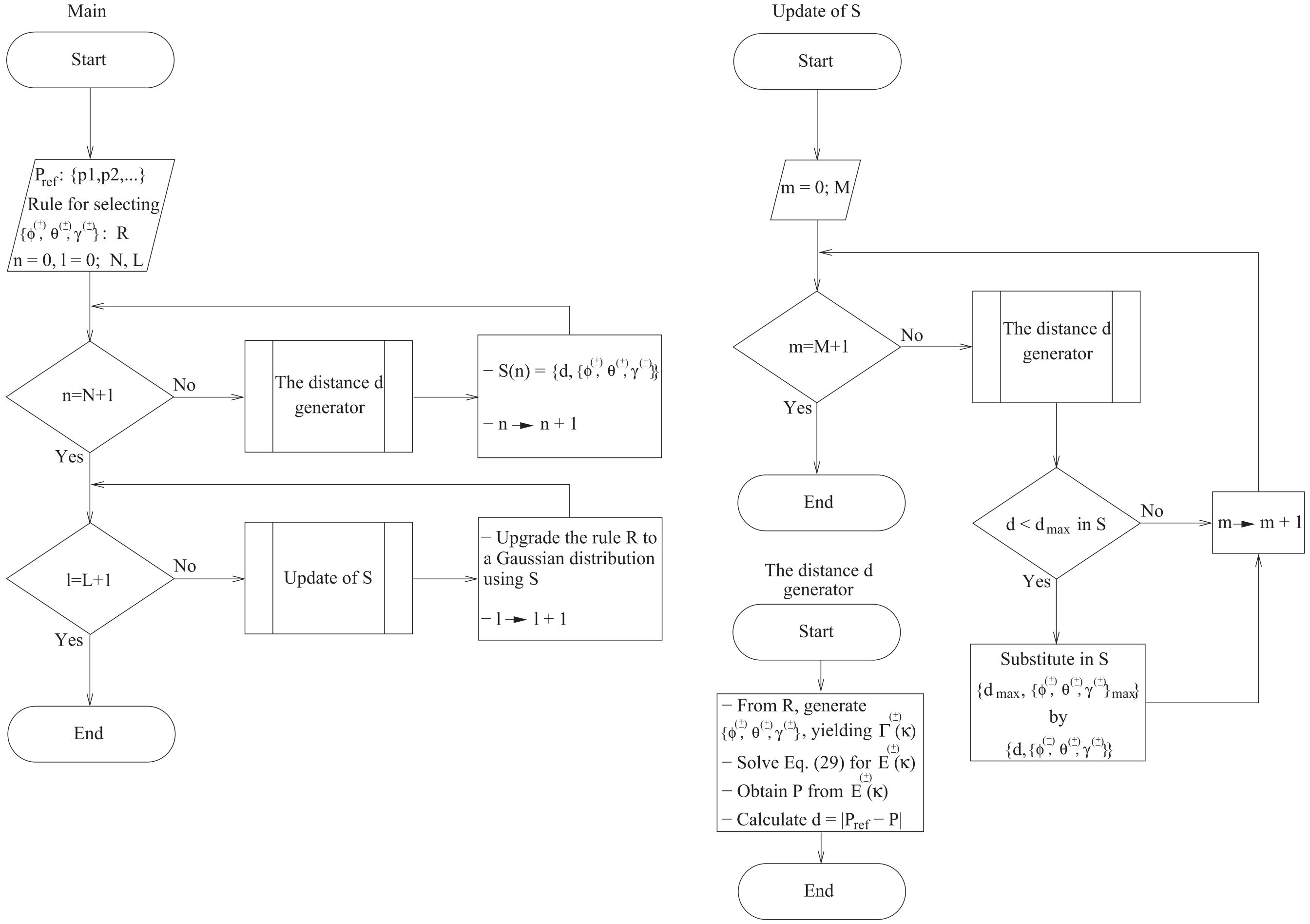

FIG. 21. Flowchart of the algorithm which numerically searches for proper matrices $\Gamma^{(\pm)}$ leading, from Eq. (29), to energy band structures closely resembling those from the *ab initio* 1 computations [36]. The protocol operational details are given by (i)–(v) in Appendix C.

$$\hat{S}^{(+)}_{\text{germ}} = \begin{pmatrix} -0.235401 - 0.234025\,i & 0.907655 + 0.00356565\,i & -0.149145 + 0.209104i \\ -0.50009 - 0.644277\,i & -0.137028 - 0.0414458\,i & 0.317586 - 0.46202\,i \\ 0.473104 + 0.0284348\,i & 0.269421 - 0.288216i & -0.218807 - 0.756195\,i \end{pmatrix},$$

$$\hat{S}^{(-)}_{\text{germ}} = \begin{pmatrix} -0.38446 - 0.0755964\,i & 0.12191 - 0.652291\,i & 0.112986 + 0.627188\,i \\ -0.316329 + 0.606195\,i & -0.105728 + 0.454626\,i & -0.352752 + 0.43608\,i \\ 0.0840718 - 0.609813\,i & -0.359216 + 0.461254\,i & 0.188915 + 0.493539\,i \end{pmatrix},$$

$$\hat{S}^{(+)}_{\text{sili}} = \begin{pmatrix} -0.107015 - 0.00798447\,i & -0.0265558 + 0.869958\,i & 0.269032 - 0.398214\,i \\ -0.690817 - 0.648893\,i & -0.0470178 + 0.0331329\,i & -0.306416 + 0.0671659\,i \\ -0.300254 + 0.0064432\,i & 0.0124119 - 0.488882\,i & 0.460001 - 0.677529\,i \end{pmatrix},$$

$$\hat{S}^{(-)}_{\text{sili}} = \begin{pmatrix} -0.457887 + 0.324023\,i & 0.538585 + 0.326047\,i & -0.533475 + 0.0661224\,i \\ -0.35892 + 0.442505\,i & -0.239453 + 0.39051\,i & 0.611317 + 0.303022\,i \\ 0.60042 + 0.0144789\,i & -0.210423 + 0.591191\,i & -0.309735 + 0.386738\,i \end{pmatrix}, \tag{B3}$$

moreover, $\gamma_{\text{graf}} = -0.398702420895367 67$, $\tilde{\varepsilon}_{\text{graf}} = -11.073477059111063$; $\gamma_{\text{germ}} = 0.309361885861335$, $\tilde{\varepsilon}_{\text{germ}} = 4.371430728147026$; $\gamma_{\text{sili}} = -0.3565029108304439$, $\tilde{\varepsilon}_{\text{sili}} = -5.38457659978849$.

APPENDIX C: THE NUMERICAL SEARCH PROCEDURE FOR $\hat{\Gamma}^{(\pm)}$

As previously mentioned, we have implemented a numerical protocol to search for proper $\Gamma^{(\pm)}$'s which, once inserted into Eq. (29), yield energy band structures closely agreeing with those from the *ab initio* 1 method [36] discussed in the main text. For the run times considered, never more than one hour for each material, the best found $\Gamma^{(\pm)}$'s are those given in Eq. (B3). The flowchart in Fig. 21 summarizes the actual algorithm. The main quantities/variables and the key stages of the procedure are the following.

(i) $P_{\rm ref} = \{p_1, \ldots, p_{\mathcal{P}_u}, p_{\mathcal{P}_u+1}, \ldots, p_{\mathcal{P}_u+\mathcal{P}_l}\}$, with $p_j = E_+(\kappa_{x,j}, \kappa_{y,j})$ if $j \leqslant \mathcal{P}_u$ and $p_j = E_-(\kappa_{x,j}, \kappa_{y,j})$ if $j > \mathcal{P}_u$, calculated from the *ab initio* 1 approach. Thus, $P_{\rm ref}$ is the reference set of $\mathcal{P} = \mathcal{P}_u + \mathcal{P}_l$ points from the upper and lower energy bands generated by *ab initio* 1. The $(\kappa_{x,j}, \kappa_{y,j})$ are fairly equally spaced along the direction of the high-symmetry points Γ, K, and M (refer to Figs. 18–20). We have set $\mathcal{P}_u = 58$, $\mathcal{P}_l = 50$ for graphene, $\mathcal{P}_u = 93$, $\mathcal{P}_l = 87$ for germanene, and $\mathcal{P}_u = 69$, $\mathcal{P}_l = 59$ for silicene.

(ii) For each pair of matrices $\Gamma^{(\pm)}$, $E(\vec{\kappa})$ results from Eq. (29). The set $P = \{E(\kappa_{x,j}, \kappa_{y,j})\}$ is computed for E either E_+ or E_- depending on j. So, the distance $d = |P_{\rm ref} - P|$ reads $d = \sqrt{\sum_j (p_j - E(\kappa_{x,j}, \kappa_{y,j}))^2}$.

(iii) To test distinct $\Gamma^{(\pm)}$'s, we randomly choose the $\theta_s^{(\pm)}$'s, $\phi_s^{(\pm)}$'s and γ (see Appendix B) values according to a specified rule R, which is upgraded in the code each time the set S is updated. For sake of discussion, consider z generically representing any one of the $\theta_s^{(\pm)}$'s, $\phi_s^{(\pm)}$'s, γ parameters. In the routine initialization, when for the first time the set S — whose elements $S(n)$ have the form $\{d, \{\theta_s^{(\pm)}, \phi_s^{(\pm)}, \gamma\}\}$ — is generated (see Fig. 21), the rule R is simply to draw z from a uniform distribution (obviously, within the proper interval of z). For the subsequent upgrades of R, the code takes the K collection of matrices parameters in S resulting in the lowest d's. For each specific parameter z, the routine calculates an average $\overline{z}_S$ and variance $\sigma_{z,S}$ over the corresponding K sample. Then, the redefined rule R becomes to sort the z's drawn from a Gaussian distribution characterized by $\overline{z}_S$ and $\sigma_{z,S}$.

(iv) Updates of S are implemented by substituting the element $S(n)$ of S presenting the largest distance quantifier, of value $d_{\rm max}$, by the parameters of a randomly created pair $\Gamma^{(\pm)}$ whenever they lead to $d < d_{\rm max}$.

(v) Lastly, the quantities N, L, M, and K, see Fig. 21, have been established by means of preliminary numerical tests (the aforementioned run times do not include such initial simulations). The values used are $N = M = 75$, $L = 6695$, $K = 13$ for graphene; $N = M = 75$, $L = 6695$, $K = 15$ for germanene; and $N = M = 75$, $L = 6695$, $K = 15$ for silicene.

Finally, we mention an extra condition, not described in the algorithm depicted in Fig. 21. Eventually, d could be small because most of the points in $P_{\rm rev}$ and P are very close together. However, a few special (but important) points, usually around Γ, K, and M, could display considerable discrepancies. So, we have assumed an additional selection rule, besides discarding those matrices leading to large d's. If d is small, but some great local variations of $|P_{\rm ref} - P|$ occur around the symmetry points, the corresponding $\Gamma^{(\pm)}$ are also eliminated. This extra exclusion is rarely employed for the graphene. But it is frequent for germanene and silicene. For example, for the about 500 000 pairs of matrices tested for germanene and silicene only, respectively, 29% and 34% showed no strong local fluctuations for the difference between the points of $P_{\rm ref}$ and P in the vicinity of Γ, K, or M. We speculate that global small d's also tend to lead to the nonexistence of strong local fluctuations of $|P_{\rm ref} - P|$ for the former but not for the two latter because although graphene does present a truly stable planar configuration, germanene and silicene do not (see the discussion in Sec. VI B).

---

[1] D. J. Thouless, M. Kohmoto, M. P. Nightingale, and M. den Nijs, Quantized Hall Conductance in a Two-Dimensional Periodic Potential, Phys. Rev. Lett. **49**, 405 (1982).

[2] J. E. Avron, R. Seiler, and B. Simon, Homotopy and Quantization in Condensed Matter Physics, Phys. Rev. Lett. **51**, 51 (1983).

[3] M. V. Berry, Quantum phase factors accompanying adiabatic changes, Proc. Royal Soc. A **392**, 45 (1984).

[4] F. D. M. Haldane, Model for a Quantum Hall Effect Without Landau Levels: Condensed-Matter Realization of the "Parity Anomaly," Phys. Rev. Lett. **61**, 2015 (1988).

[5] M. I. Monastyrsky, *Topology in Condensed Matter* (Springer, Berlin, 2006).

[6] A. Altland and B. D. Simons, *Condensed Matter Field Theory* (Cambridge University Press, Cambridge, 2010).

[7] F. Ortmann, S. Roche, and S. O. Velenzuela, *Topological Insulators: Fundamentals and Perspectives* (John Wiley & Sons, Weinheim, 2015).

[8] C. Chamon, M. O. Goerbig, R. Moessner, and L. F. Cugliandolo, *Topological Aspects of Condensed Matter Physics* (Oxford University Press, Oxford, 2017).

[9] S. Q. Shen, The family of topological phases in condensed matter, Nat. Sci. **1**, 49 (2014).

[10] X. G. Wen, Zoo of quantum-topological phases of matter, Rev. Mod. Phys. **89**, 041004 (2017).

[11] J. Liu, A short review on first-principles study of gapped topological materials, Comput. Mater. Sci. **195**, 110467 (2021).

[12] D. Culcer, A. C. Keser, Y. Li, and G. Tkachov, Transport in two-dimensional topological materials: Recent developments in experiment and theory, 2D Mater. **7**, 022007 (2020).

[13] S. Gupta and A. Saxena, A topological twist on materials science, MRS Bull. **39**, 265 (2014).

[14] M. G. Vergniory, L. Elcoro, C. Felser, N. Regnault, B. A. Bernevig, and Z. Wang, A complete catalogue of high-quality topological materials, Nature (London) **566**, 480 (2019).

[15] A. R. Ashrafi and M. V. Diudea, *Distance, Symmetry, and Topology in Carbon Nanomaterials* (Springer, Cham, 2016).

[16] P. Bondavalli, *2D Materials: and Their Exotic Properties* (De Gruyter, Berlin, 2022).

[17] M. Ashton, J. Paul, S. B. Sinnott, and R. G. Hennig, Topology-Scaling Identification of Layered Solids and Stable Exfoliated 2D Materials, Phys. Rev. Lett. **118**, 106101 (2017).

[18] Z. Song, T. Zhang, Z. Fang, and C. Fang, Quantitative mappings between symmetry and topology in solids, Nat. Commun. **9**, 3530 (2018).

[19] X. Zou, Y. Xu, and W. Duan, 2D materials: Rising star for future applications, Innov. **2**, 100115 (2021).

[20] M. Geier, L. Trifunovic, M. Hoskam, and P. W. Brouwer, Second-order topological insulators and superconductors with an order-two crystalline symmetry, Phys. Rev. B **97**, 205135 (2018).

[21] K. S. Novoselov, A. K. Geim, S. V. Morozov, D. Jiang, M. I. Katsnelson, I. V. Grigorieva, S. V. Dubonos, and A. A. Firsov, Two-dimensional gas of massless Dirac fermions in graphene, Nature (London) **438**, 197 (2005).

[22] D. Li and R. B. Kaner, Graphene-based materials, Science **320**, 1170 (2008).

[23] A. K. Geim, Graphene: Status and prospects, Science **324**, 1530 (2009).

[24] A. H. C. Neto, F. Guinea, N. M. R. Peres, K. S. Novoselov, and A. K. Geim, The electronic properties of graphene, Rev. Mod. Phys. **81**, 109 (2009).

[25] M. J. Allen, V. C. Tung, and R. B. Kaner, Honeycomb carbon: A review of graphene, Chem. Rev. **110**, 132 (2010).

[26] E. Kan, Z. Li, and J. Yang, Graphene nanoribbons: Geometric, electronic, and magnetic properties, in *Physics and Applications of Graphene*, edited by S. Mikhailov (IntechOpen, Rijeka, 2011).

[27] A. H. C. Neto and K. S. Novoselov, New directions in science and technology: Two-dimensional crystals, Rep. Prog. Phys. **74**, 082501 (2011).

[28] V. Berry, Impermeability of graphene and its applications, Carbon **62**, 1 (2013).

[29] L. E. F. Torres, S. Roche, and J. C. Charlier, *Introduction to Graphene-Based Nanomaterials: From Electronic Structure to Quantum Transport* (Cambridge University Press, Cambridge, 2020).

[30] H. S. Arora, R. Polski, Y. Zhang, A. Thomson, Y. Choi, H. Kim, Z. Lin, I. Z. Wilson, X. Xu, J. Chu *et al.*, Superconductivity in metallic twisted bilayer graphene stabilized by WSe_2, Nature (London) **583**, 379 (2020).

[31] B. Wang, T. Ruan, Y. Chen, F. Jin, L. Peng, Y. Zhou, D. Wang, and S. Dou, Graphene-based composites for electrochemical energy storage, Energy Stor. Mater. **24**, 22 (2020).

[32] R. You, Y. Liu, Y. Hao, D. Han, Y. Zhang, and Z. You, Laser fabrication of graphene-based flexible electronics, Adv. Mater. **32**, 1901981 (2020).

[33] A. Cortijo, F. Guinea, and M. A. H. Vozmediano, Geometrical and topological aspects of graphene and related materials, J. Phys. A: Math. Theor. **45**, 383001 (2012).

[34] T. O. Wehling, A. M. Black-Schaffer, and A. V. Balatsky, Dirac materials, Adv. Phys. **63**, 1 (2014).

[35] G. G. Guzmán-Verri and L. C. Lew Yan Voon, Electronic structure of silicon-based nanostructures, Phys. Rev. B **76**, 075131 (2007).

[36] N. J. Roome and J. D. Carey, Beyond graphene: Stable elemental monolayers of silicene and germanene, ACS Appl. Mater. Interfaces **6**, 7743 (2014).

[37] A. Feyzi and R. Chegel, Heat capacity, electrical and thermal conductivity of silicene, Eur. Phys. J. B **89**, 193 (2016).

[38] M. H. Rahman, S. Mitra and D. A. Redwan, Electronic band structure of group IV 2D materials: Graphene, silicene, germanene, stanene using tight binding approach, in *2020 2nd International Conference on Advanced Information and Communication Technology (ICAICT)* (IEEE, 2020), pp. 207–212.

[39] J. M. Soler, E. Artacho, J. D. Gale, A. García, J. Junquera, P. Ordejón, and D. Sánchez-Portal, The SIESTA method for ab initio order-N materials simulation, J. Phys.: Condens. Matter **14**, 2745 (2002).

[40] A. V. Akimov and O. V. Prezhdo, Large-scale computations in chemistry: A bird's eye view of a vibrant field, Chem. Rev. **115**, 5797 (2015).

[41] K. K. Gomes, W. Mar, W. Ko, F. Guinea, and H. C. Manoharan, Designer Dirac fermions and topological phases in molecular graphene, Nature (London) **483**, 306 (2012).

[42] J. Wang, S. Deng, Z. Liu, and Liu. Z, The rare two-dimensional materials with Dirac cones, Natl. Sci. Rev. **2**, 22 (2015).

[43] N. T. T. Tran, S. Lin, C. Lin, and M. Lin, *Geometric and Electronic Properties of Graphene-Related Systems Chemical Bonding Schemes* (CRC Press, Boca Raton, 2018).

[44] I. G. Karafyllidis, Quantum walks on graphene nanoribbons using quantum gates as coins, J. Comput. Sci. **11**, 326 (2015).

[45] H. Bougroura, H. Aissaoui, N. Chancellor, and V. Kendon, Quantum-walk transport properties on graphene structures, Phys. Rev. A **94**, 062331 (2016).

[46] B. F. Venancio and M. G. E. da Luz, Construction of distinct discrete time scattering quantum walk formulations on the honeycomb lattice, Ann. Phys. **396**, 517 (2018).

[47] J. Mareš, J. Novotný, and I. Jex, Quantum walk transport on carbon nanotube structures, Phys. Lett. A **15**, 126302 (2020).

[48] Y. Aharonov, L. Davidovich, and N. Zagury, Quantum random walks, Phys. Rev. A **48**, 1687 (1993).

[49] A. M. Childs, E. Farhi, and S. Gutmann, An example of the difference between quantum and classical random walks, Quantum Inf. Process. **1**, 35 (2002).

[50] J. Kempe, Quantum random walks: An introductory overview, Contemp. Phys. **44**, 307 (2003).

[51] N. Konno, Quantum walks, in *Quantum Potential Theory*, edited by U. Franz and M. Schürmann (Springer, Berlin, 2008).

[52] C. M. Chandrashekar and R. Laflamme, Quantum phase transition using quantum walks in an optical lattice, Phys. Rev. A **78**, 022314 (2008).

[53] A. Ahlbrecht, A. Alberti, D. Meschede, V. B. Scholz, A. H. Werner, and R. F. Werner, Molecular binding in interacting quantum walks, New J. Phys. **14**, 073050 (2012).

[54] C. Fábri and A. G. Császár, Vibrational quantum graphs and their application to the quantum dynamics of CH_5+, Phys. Chem. Chem. Phys. **20**, 16913 (2018).

[55] P. Chawla and C. M. Chandrashekar, Quantum walks in polycyclic aromatic hydrocarbons, New J. Phys. **23**, 113013 (2021).

[56] J. C. F. Matthews and M. G. Thompson, Quantum optics: An entangled walk of photons, Nature (London) **484**, 47 (2012).

[57] F. Cardano, F. Massa, H. Qassim, E. Karimi, S. Slussarenko, D. Paparo, C. Lisio, F. Sciarrino, E. Santamato, R. W. Boyd, and L. Marrucci, Quantum walks and wavepacket dynamics on a lattice with twisted photons, Sci. Adv. **1**, e1500087 (2015).

[58] L. C. Botten, N. A. Nicorovici, R. C. McPhedran, C. Martijn de Sterke, and A. A. Asatryan, Photonic band structure calculations using scattering matrices, Phys. Rev. E **64**, 046603 (2001).

[59] S. E. Venegas-Andraca, *Quantum Walks for Computer Scientists* (Springer, Cham, 2008).

[60] R. Portugal, *Quantum walks and Search Algorithms* (Springer, New York, 2013).

[61] H. S Ghizoni and E. P. M. Amorim, Trojan quantum walks, Braz. J. Phys. **49**, 168 (2019).

[62] K. Kadian, S. Garhwal, and A. Kumar, Quantum walk and its application domains: A systematic review, Comput. Sci. Rev. **41**, 100419 (2021).

[63] C. Lyu, L. Yu, and S. Wu, Localization in quantum walks on a honeycomb network, Phys. Rev. A **92**, 052305 (2015).

[64] Focus on the topological properties of 2D layered materials (Special Issue), edited by S. Dong, D. Xiao, and S. Wu, 2D Mater. **6** (2018).

[65] M. Hillery, J. Bergou, and E. Feldman, Quantum walks based on an interferometric analogy, Phys. Rev. A **68**, 032314 (2003).

[66] E. Feldman and M. Hillery, Scattering theory and discrete-time quantum walks, Phys. Lett. A **324**, 277 (2004).

[67] B. F. Venancio, F. M. Andrade, and M. G. E. da Luz, Unveiling and exemplifying the unitary equivalence of discrete time quantum walk models, J. Phys. A **46**, 165302 (2013).

[68] F. M. Andrade and M. G. E. da Luz, Equivalence between discrete quantum walk models in arbitrary topologies, Phys. Rev. A **80**, 052301 (2009).

[69] S. E. Venegas-Andraca, Quantum walks: A comprehensive review, Quantum Inf. Process. **11**, 1015 (2012).

[70] S. Karimi, E. Helal, G. Gutierrez, N. Moghimian, M. Madinehei, E. David, M. Samara, and N. Demarquette, A review on graphene's light stabilizing effects for reduced photodegradation of polymers, Crystals **11**, 3 (2021).

[71] L. K. Grover, A fast quantum mechanical algorithm for database search, in *Proceedings of the Twenty-Eighth Annual ACM Symposium on Theory of Computing* (Association for Computing Machinery, New York, 1996).

[72] A. M. Childs and J. Goldstone, Spatial search by quantum walk, Phys. Rev. A **70**, 022314 (2004).

[73] N. B. Lovett, S. Cooper, M. Everitt, M. Trevers, and V. Kendon, Universal quantum computation using the discrete-time quantum walk, Phys. Rev. A **81**, 042330 (2010).

[74] F. Magniez, A. Nayak, J. Roland, and M. Santha, Search via quantum walk, SIAM J. Comput. **40**, 142 (2011).

[75] N. W. Ashcroft and N. D. Mermin, *Solid State Physics* (Saunders Collage Publishing, Philadelphia, 1976).

[76] S. Tang and M. S. Dresslhaus, Constructing a large variety of Dirac-cone materials in the $\mathrm{Bi}_{1\text{-}x}\mathrm{Sb}_x$ thin film system, Nanoscale **4**, 7786 (2012).

[77] E. Kalesaki, C. Delerue, C. M. Smith, W. Beugeling, G. Allan, and D. Vanmaekelbergh, Dirac Cones, Topological Edge States, and Nontrivial Flat Bands in Two-Dimensional Semiconductors with a Honeycomb Nanogeometry, Phys. Rev. X **4**, 011010 (2014).

[78] A. Das and S. Pujari, SU(3) fermions in a three-band graphene-like model, Phys. Rev. B **100**, 125152 (2019).

[79] V. P. Gerdt, Y. G. Palli, and A. M. Khvedelidze, Light-cone Yang-Mills mechanisms: SU(2) vs. SU(3), Theor. Math. Phys. **155**, 557 (2008).

[80] P. R. Wallace, The band theory of graphite, Phys. Rev. **71**, 622 (1947).

[81] S. Das Sarma, S. Adam, E. H. Hwang, and E. Rossi, Electronic transport in two-dimensional graphene, Rev. Mod. Phys. **83**, 407 (2011).

[82] M. Ali, X. Pi, Y. Liu, and D. Yang, Electronic and magnetic properties of graphene, silicene and germanene with varying vacancy concentration, AIP Adv. **7**, 045308 (2017).

[83] V. Zolyomi, N. D. Drummond, J. R. Wallbank, and V. Falko, Density-functional and tight-binding theory of silicene and silicane, in *Silicene: Prediction, Synthesis, Application*, edited by P. Vogt and G. Le Lay (Springer, Cham, 2018).

[84] S. Reich, J. Maultzsch, C. Thomsen, and P. Ordejon, Tight-binding description of graphene, Phys. Rev. B **66**, 035412 (2002).

[85] K. Wakabayashi, Y. Takane, M. Yamamoto, and M. Sigrist, Electronic transport properties of graphene nanoribbons, New J. Phys. **11**, 095016 (2009).

[86] D. R. Cooper, B. D'Anjou, N. Ghattamaneni, B. Harack, M. Hilke, A. Horth, N. Majlis, M. Massicotte, L. Vandsburger, E. Whiteway *et al.*, Experimental review of graphene, Int. Sch. Res. Notices **2012**, 501686 (2012).

[87] C. Thomsen and S. Reich, Double Resonant Raman Scattering in Graphite, Phys. Rev. Lett. **85**, 5214 (2000).

[88] R. Saito, A. Jorio, A. G. Souza Filho, G. Dresselhaus, M. S. Dresselhaus, and M. A. Pimenta, Probing Phonon Dispersion Relations of Graphite by Double Resonance Raman Scattering, Phys. Rev. Lett. **88**, 027401 (2001).

[89] A. Jorio, M. S. Dresselhaus, R. Saito, and G. Dresselhaus, *Raman Spectroscopy in Graphene Related Systems* (John Wiley & Sons, Weinheim, 2011).

[90] M. S. Dresselhaus, G. Dresselhaus, K. Sugihara, I. L. Spain, and H. A. Goldberg, *Graphite Fibers and Filaments* (Springer, Berlin, 2013).

[91] G. S. Painter and D. E. Ellis, Electronic band structure and optical properties of graphite from a variational approach, Phys. Rev. B **1**, 4747 (1970).

[92] D. Coello-Fiallos, T. Tene, J. L. Guayllas, D. Haro, A. Haro, and C. Vacacela Gomez, DFT comparison of structural and electronic properties of graphene and germanene: Monolayer and bilayer systems, Mater. Today **4**, 6835 (2017).

[93] P. Narang, L. Zhao, S. Claybrook, and R. Sundararaman, Effects of interlayer coupling on hot-carrier dynamics in graphene-derived van der Waals heterostructures, Adv. Opt. Mater. **5**, 1600914 (2017).

[94] N. Marzari, A. A. Mostofi, J. R. Yates, I. Souza, and D. Vanderbilt, Maximally localized Wannier functions: Theory and applications, Rev. Mod. Phys. **84**, 1419 (2012).

[95] S. K. Sahoo and K. Wei, A perspective on recent advances in 2D stanene nanosheets, Adv. Mater. Interfaces **6**, 1900752 (2019).

[96] A. Kara, H. Enriquez, A. P. Seitsonen, L. C. Lew, Yan Voon, S. Vizzini, B. Aufray, and H. Oughaddou, A review on silicene—new candidate for electronics, Surf. Sci. Rep. **67**, 1 (2012).

[97] Y. Ding and J. Ni, Electronic structures of silicon nanoribbons, Appl. Phys. Lett. **95**, 083115 (2009).

[98] C. Liu, H. Jiang, and Y. Yao, Low-energy effective Hamiltonian involving spin-orbit coupling in silicene and two-dimensional germanium and tin, Phys. Rev. B **84**, 195430 (2011).

[99] X. Yang and J. Ni, Electronic properties of single-walled silicon nanotubes compared to carbon nanotubes, Phys. Rev. B **72**, 195426 (2005).

[100] J. B. Bronzan, Parametrization of SU (3), Phys. Rev. D **38**, 1994 (1988).

[101] S. Cahangirov, M. Topsakal, E. Aktürk, H. Şahin, and S. Ciraci, Two-and One-Dimensional Honeycomb Structures of Silicon and Germanium, Phys. Rev. Lett. **102**, 236804 (2009).

[102] A. Stpniak-Dybala, P. Dyniec, M. Kopciuszyski, R. Zdyb, M. Jałochowski, and M. Krawiec, Planar silicene: A new silicon allotrope epitaxially grown by segregation, Adv. Funct. Mater. **29**, 1906053 (2019).

[103] S. Lebègue and O. Eriksson, Electronic structure of two-dimensional crystals from *ab initio* theory, Phys. Rev. B **79**, 115409 (2009).

[104] S. Wang, A comparative first-principles study of orbital hybridization in two-dimensional C, Si, and Ge, Phys. Chem. Chem. Phys. **13**, 11929 (2011).

[105] S. Trivedi, A. Srivastava, and R. Kurchania, Silicene and germanene: A first principle study of electronic structure and effect of hydrogenation-passivation, J. Comput. Theor. Nanosci. **11**, 781 (2014).

[106] G. R. Bhimanapati, Z. Lin, V. Meunier, Y. Jung, J. Cha, S. Das, D. Xiao, Y. Son, M. S. Strano, V. R. Cooper *et al.*, Recent advances in two-dimensional materials beyond graphene, ACS Nano **9**, 11509 (2015).

[107] X. Du, I. Skachko, A. Barker, and E. Y. Andrei, Approaching ballistic transport in suspended graphene, Nat. Nanotechnol. **3**, 491 (2008).

[108] K. Ando, H. Isozaki, E. Korotyaev, and H. Morioka, Inverse scattering on the quantum graph for graphene, arXiv:2102.05217.

[109] S. Lehtola and H. Jónsson, Unitary optimization of localized molecular orbitals, J. Chem. Theory Comput. **9**, 5365 (2013).

[110] M. Hendzel, M. Fidrysiak, and J. Spałek, Toward complementary characterization of the chemical bond, J. Phys. Chem. Lett. **13**, 10261 (2022).

[111] S. Kitou, Y. Hosogi, R. Kitaura, T. Naito, T. Nakamura, and H. Sawa, Direct observation of molecular orbitals using synchrotron x-ray diffraction, Crystals **10**, 998 (2020).

[112] N. Watanabe, S. Yamada, and M. Takahashi, Relation between the spatial shape of excited molecular orbital and molecular-frame electron scattering cross section, J. Phys.: Conf. Ser. **1412**, 142017 (2020).

[113] M. Liscidini, D. Gerace, L. C. Andreani, and J. E. Sipe, Scattering-matrix analysis of periodically patterned multilayers with asymmetric unit cells and birefringent media [Phys. Rev. B 77, 035324 (2008)], Phys. Rev. B **77**, 199904(E) (2008).

[114] K. Nakada, M. Fujita, G. Dresselhaus, and M. S. Dresselhaus, Edge state in graphene ribbons: Nanometer size effect and edge shape dependence, Phys. Rev. B **54**, 17954 (1996).